

CANCER

Single-cell multimodal analysis reveals tumor microenvironment predictive of treatment response in non–small cell lung cancer

Yuanning Zheng¹, Christoph Sadée¹, Michael Ozawa², Brooke E. Howitt², Olivier Gevaert^{1,3*}

Non–small cell lung cancer (NSCLC) constitutes over 80% of lung cancer cases and remains a leading cause of cancer-related mortality worldwide. Despite the advent of immune checkpoint inhibitors, their efficacy is limited to 27 to 45% of patients. Identifying likely treatment responders is essential for optimizing healthcare and improving quality of life. We generated multiplex immunofluorescence (mIF) images, histopathology, and RNA sequencing data from human NSCLC tissues. Through the analysis of mIF images, we characterized the spatial organization of 1.5 million cells based on the expression levels for 33 biomarkers. To enable large-scale characterization of tumor microenvironments, we developed NucSegAI, a deep learning model for automated nuclear segmentation and cellular classification in histology images. With this model, we analyzed the morphological, textural, and topological phenotypes of 45.6 million cells across 119 whole-slide images. Through unsupervised phenotype discovery, we identified specific lymphocyte phenotypes predictive of immunotherapy response. Our findings can improve patient stratification and guide selection of effective therapeutic regimens.

Copyright © 2025 The Authors, some rights reserved; exclusive licensee American Association for the Advancement of Science. No claim to original U.S. Government Works. Distributed under a Creative Commons Attribution NonCommercial License 4.0 (CC BY-NC).

INTRODUCTION

Lung cancers remain the leading cause of cancer-related deaths globally, with non–small cell lung cancer (NSCLC) accounting for over 80% of cases (1). Both systemic and nonsystemic therapeutic approaches have been used to manage the disease. Surgery remains one of the major curative treatments for early-stage NSCLC cases with resectable malignancy. Unfortunately, ~30 to 55% of patients experience recurrence and succumb to their disease, even after complete resection (2, 3). Recurrence can occur rapidly, with 50 to 90% of cases detected within 2 years of surgery and 90 to 95% within the first 5 years (4).

Following NSCLC recurrence, only a small proportion of patients are eligible for additional surgery, whereas most are treated with radiation and/or systemic therapies (5). Although platinum-based chemotherapy has been a standard systemic treatment, its side effects, such as nonspecific cytotoxicity and drug resistance, have posed critical clinical challenges (6). Over the past decade, immune checkpoint inhibitors (ICIs) have revolutionized the therapeutic landscape for NSCLC. In patients without targetable oncogenic driver mutations, anti-PD-1/PD-L1 antibodies have become the cornerstone of ICI treatment (7, 8). By inhibiting the interaction between the programmed cell death 1 (PD-1) receptor and its ligand PD-L1, these antibodies activate the adaptive immune response against cancer cells. Although several anti-PD-1/PD-L1 antibodies have demonstrated clinical benefit (7–10), the objective response rate ranges from 27 to 45%, indicating that the treatment benefit is limited to a subset of patients (11–14). Identifying reliable biomarkers able to predict treatment response is essential for determining the most likely effective therapeutic strategies at the individual patient level.

Currently available predictive biomarkers for anti-PD-1/PD-L1 treatment include PD-L1 expression levels assessed by immunohistochemistry (IHC) (15), tumor mutation burden (16), and micro-

satellite stability (17). The US Food and Drug Administration has approved several PD-L1 IHC assays as companion or complementary diagnostic tools for NSCLC (15). However, the predictive performance varies across different clinical trials. Although earlier studies suggest improved responsiveness in patients with higher PD-L1 expression levels, recent studies have revealed a lack of strong associations (9, 18). Moreover, intra- and interobserver variabilities for PD-L1 scoring can cause inconsistent evaluation of a patient's eligibility for ICI treatment (19).

Interpatient variability in response to NSCLC treatments is largely driven by cancer heterogeneity, with the tumor microenvironment (TME) as a major contributor. The TME consists of a complex repertoire, including immune cells, fibroblasts, blood vessels, signaling molecules, and extracellular matrix. Signaling interactions between cancer cells and their microenvironment affect cell metabolism, proliferation, and apoptosis (20, 21). Thus, combining the PD-L1 expression levels and tumor microenvironmental features may improve the efficacy for predicting treatment response. Earlier studies have relied on IHC analyses to characterize the TME (22–24). However, many of these studies focused on investigating the distribution of individual protein markers (e.g., CD8 and CD68), which overlook the complex spatial cellular organization within tumor tissues. To address this challenge, recent studies have used multiplexed tissue imaging technologies that enable simultaneous, multiparametric quantification of biomarker expression levels for a tissue section (25–29). Sorin *et al.* profiled 1.6 million cells in lung adenocarcinoma using imaging mass cytometry with 35 antibodies, linking B cell-enriched neighborhoods to prolonged overall survival (30). A recent study by Enfield *et al.* revealed a significant association between neutrophil infiltration and risk of disease relapse and metastasis after surgery (31). Monkman *et al.* focused on the multiplex imaging analysis of 35 patients with NSCLC who received immunotherapy, and their results linked regulatory T (T_{reg}) cells to unfavorable immunotherapy response (32). A conventional approach to multiplexed tissue profiling involves selecting regions of interest (ROIs) and assembling them into tissue microarrays (TMAs). The diameter of a TMA

¹Stanford Center for Biomedical Informatics Research, Department of Medicine, Stanford University, Stanford, CA 94305, USA. ²Department of Pathology, Stanford University, Stanford, CA 94305, USA. ³Department of Biomedical Data Science, Stanford University, Stanford, CA 94305, USA.

*Corresponding author. Email: ogevaert@stanford.edu

core typically ranges from 0.6 to 2.0 mm. Many existing studies are limited by profiling only a single region per tumor, capturing a relatively small number of cells. Given the known intratumoral heterogeneity in NSCLC, how spatial cellular architectures are associated with immunotherapy response remains incompletely understood.

Although multiplex imaging technologies offer valuable insights into tissue architecture and cell-type distribution, their implementation is resource intensive, requiring specialized laboratory equipment and highly trained personnel. Current approaches predominantly rely on multiplexed antibody labeling or high-throughput sequencing, both of which limit widespread adoption in clinical settings due to cost and technical complexity (25–28). In contrast, hematoxylin and eosin (H&E)-stained histology images are relatively inexpensive to obtain and already exist for diagnostic purposes as part of patient care. Recent advancements in digital pathology have enabled the digitization of whole-slide images (WSIs), allowing for high-resolution visualization of cellular morphology and tissue architecture. As a result, histology images can provide a complementary perspective on the TME, providing additional insights alongside multiplex spatial imaging techniques.

In this study, we hypothesize that integrating tumor microenvironmental information from multimodal biomedical datasets can guide the selection of effective treatment regimens. To test this hypothesis, we generated tissue-matched multiplex immunofluorescence (mIF) images, whole-slide histology images, and RNA sequencing (RNA-seq) data of tumors from patients with NSCLC. To identify clinically relevant spatial cellular architectures, we modeled the TME at a single-cell resolution using advanced spatial statistical algorithms. The results identified image-based biomarkers for treatment responsiveness, which can improve patient stratification and guide personalized therapeutic strategies.

RESULTS

Characterize clinically relevant tissue microenvironments in NSCLC using mIF

Tumor tissues from a cohort of patients with NSCLC ($n = 132$) were collected from Stanford Medical Center during diagnosis or surgery, with clinical characteristics summarized in table S1. The cohort contains 76 females and 56 males, and the median follow-up time is 3.6 years (interquartile range: 796 to 1876 days). The cohort covers main histological class of NSCLC, including 94 patients with adenocarcinomas (LUAD) and 32 with squamous cell carcinomas (LUSC). Among the entire cohort, whole-slide histology images were available for 115 patients and RNA-seq data for 122 patients (fig. S1). To enable a detailed characterization of the tissue microenvironment, we performed mIF imaging analysis using the PhenoCycler platform on tumors from 50 patients. Unlike existing studies where only one small tumor region was selected for downstream analysis (32, 33), we used a multiregion sampling approach to select at least two distinct 1-mm² regions from each tumor. These selected regions were then arranged into TMAs (255 tissue cores) (Fig. 1A). This multiregion sampling strategy allowed us to reliably assess the extent of spatial heterogeneity within individual tumor tissues. Tissues were stained with a panel of 33 antibodies, including 19 cell lineage markers, 6 costimulatory/inhibitory markers, 4 immune signaling markers, and 4 tissue structural markers (table S2). On the basis of the protein expression levels, we classified 1.5 million cells into 13 cell types using a hierarchical lineage assignment strategy (Fig. 1B and fig. S2, A

to C) (30). The Pan-cytokeratin positive (PanCK+) cells were further classified into tumor or benign cells based on pathologists' examination of histology images. Because benign cells are not expected to affect clinical outcomes, we excluded them from downstream analysis. Overall, immune cell infiltration was detected in all NSCLC tissues, with the exact cell-type proportions varying across the patients, highlighting both intratumoral and interpatient heterogeneity (Fig. 1C and fig. S3A). By comparing the cell-type proportions in histologically distinct NSCLC tissues using a linear mixed-effect model (LMM), we found that LUSC had a significantly increased proportion of B cells and monocytes compared to LUAD (Fig. 1D and fig. S3B, LMM, $P < 0.05$). In contrast, LUAD had higher proportions of T helper (T_H) cells, dendritic cells (Dc) and vascular cells ($P < 0.05$). By comparing cell-type proportions in tumors from late-stage cancers (stages III to IV) to those from the early stage (stages I to II), we found that late-stage tumors had significantly higher proportions of tumor cells (Fig. 1D and fig. S3C, $P = 0.03$). No significant differences were observed for the proportions of other cell types across different cancer stages. In addition, we did not find any significant associations between cell-type proportions and smoking history.

Within tumor tissues, a single cell does not function alone but forms complex signaling interactions with neighboring cells. The multicellular community collectively drives tumor progression, metastasis, and resistance to therapy (34, 35). To identify recurrent phenotypes of spatial cellular neighborhoods across tumor tissues, we analyzed the cell-type composition within the neighborhood of each cell (Materials and Methods). The neighborhood of a cell was defined as its surrounding cells located within 50 μm (Fig. 1A). Using unsupervised clustering analysis, we identified eight distinct neighborhood phenotypes (Fig. 1, E and F, and fig. S4A). These included neighborhoods enriched with tumor cells ("Tumor_core"), neighborhoods containing both tumor cells and lymphocytes ("Tumor_lymph"), neighborhoods containing a mixture of different lymphocyte subsets ("Mixed_lymph"), and neighborhoods enriched with macrophages ("Macrophage_enriched"), cytotoxic T (Tc) cells ("Tc_enriched"), fibroblasts ("Fibro_enriched"), monocytes ("Monocyte_enriched"), or vascular cells ("Vasc_enriched"). The proportion of cells within Monocyte_enriched neighborhood was significantly increased in LUSC compared to LUAD (fig. S4, B and C, LMM, $P = 0.007$), whereas the proportion of Tumor_lymph was significantly decreased in LUSC ($P = 0.04$). In addition, the proportion of Tumor_lymph was significantly decreased in tumors from former smokers compared to never smokers (fig. S4B, LMM, $P = 0.01$).

To identify clinically relevant spatial cellular neighborhoods, we first assessed the association between neighborhood proportions and the risk of postsurgical progression. Tumors were classified as progressing if patients developed locoregional recurrence or distant metastasis after surgery (153 cores from 23 patients), whereas the remaining tumors were classified as nonprogressing (66 cores from 17 patients). The median time to progression was 14.4 months (interquartile range: 7.9 to 18.2 months). Among nonprogressing tumors, the shortest follow-up time was 33 months. By comparing the average proportions of cells assigned to each neighborhood phenotype between progressing and nonprogressing tumors, we found that progressing tumors had a significantly decreased proportion of the Tumor_lymph neighborhood (Fig. 1, G and H, and fig. S4D, 17.0% versus 26.0%, $P = 0.04$). In contrast, the average proportion of Macrophage_enriched neighborhood was significantly increased in progressing tumors (Fig. 1, G and H, 9.4% versus 7.2%, $P = 0.03$).

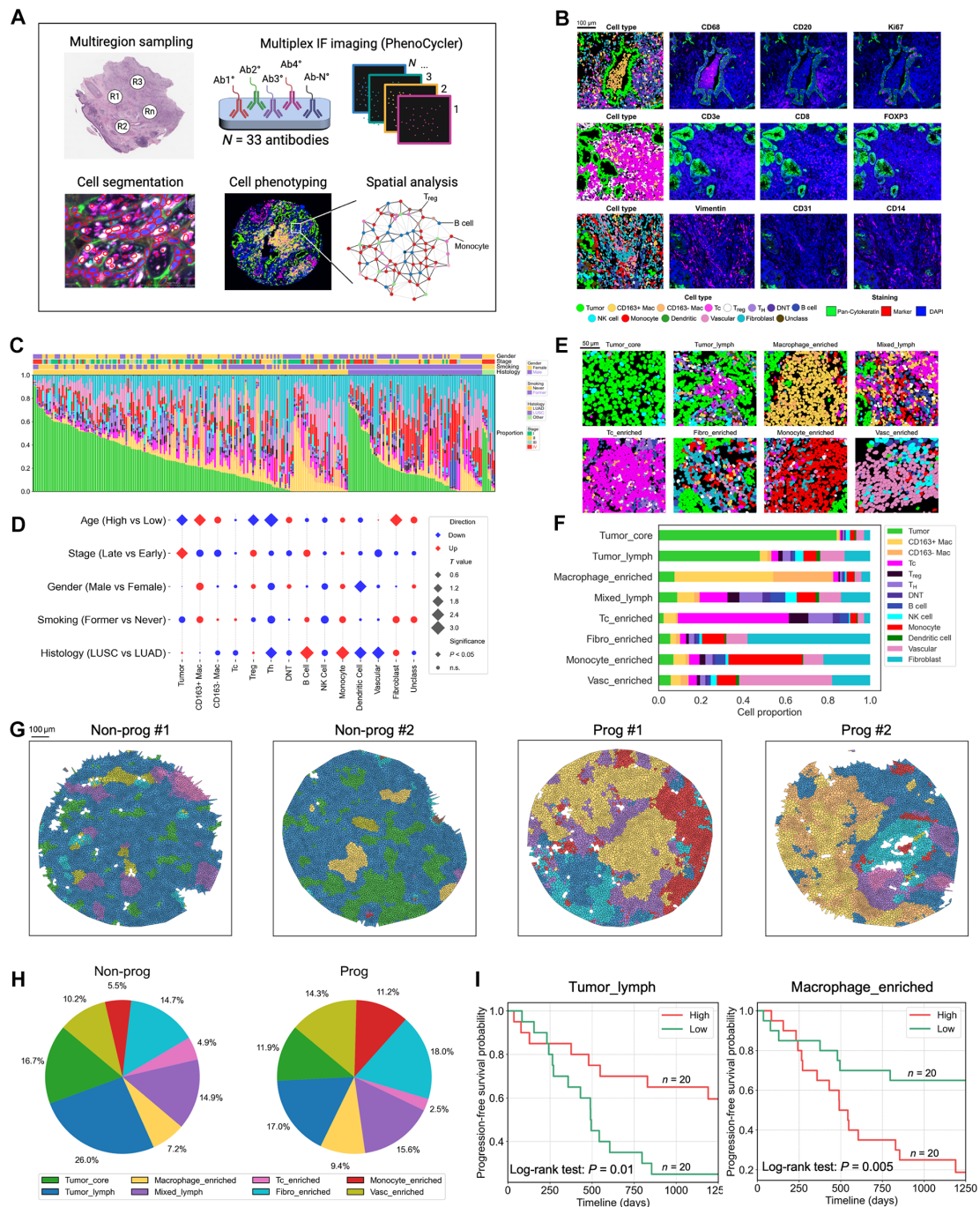


Fig. 1. Characterize NSCLC tissue microenvironment using mIF imaging. (A) Schematic representation of the mIF assay. Selected tumor regions were arranged into TMAs. Tissues were stained with a panel of 33 antibodies, and the immunofluorescence signals were captured for each cell. (B) Example regions with cell-type annotations and corresponding immunofluorescence signals. (C) Cell-type proportions across tumor tissues ($n = 255$ cores from 50 patients), organized by histological classification. Cell types are color coded according to (F). (D) Associations between cell-type proportions and clinical features. Color represents the directionality of the clinical variable (rows) in which the cell type (columns) is enriched, whereas the marker size corresponds to the T value. Significant associations are indicated by diamonds, whereas non-significant associations (n.s.) are represented by circles. Both T and P values were derived from an LMEM, with cell-type proportions as the dependent variable, clinical features as a fixed effect, and patients as a random effect. (E) Representative crops depicting the cell-type composition in each recurrent spatial neighborhood phenotype. Cells are color coded according to (B). (F) Stacked bar graph showing the average cell-type composition across the neighborhoods. (G) Representative tissue core profiles from progressing or nonprogressing tumors. Each cell is color coded by its neighborhood membership according to the legend in (H). (H) Average neighborhood proportions in progressing ($n = 153$ cores/23 patients) and nonprogressing tumors ($n = 66$ cores/17 patients). (I) Kaplan-Meier curves depicting progression-free survival for patients with high or low proportions of Tumor_lymph and Macrophage_enriched neighborhoods. Neighborhood proportions from multiple cores were averaged to summarize at the patient level, and the cohort is stratified based on the median proportion. Survival curves were compared using the log-rank test. Mac, macrophage; Tc, cytotoxic T cell; T_{reg}, regulatory T cell; T_H, T helper cell, DNT, double-negative T cell; NK, natural killer cell.

No significant differences were observed in the proportions of other neighborhood phenotypes between the progressing and nonprogressing groups. Consistent with this, patients with higher average proportions of the Tumor_lymph neighborhood within the TME demonstrated extended progression-free survival compared to those with lower proportions (Fig. 1I, log-rank test, $P = 0.01$). Conversely, patients with higher proportions of the Macrophage_enriched neighborhood had significantly shorter progression-free survival (Fig. 1I, log-rank test, $P = 0.005$).

To determine which neighborhood phenotypes were independently associated with the risk for postsurgical progression, we performed Cox regression analysis by incorporating the cancer stage, histologic class, age, gender, and smoking status as covariates into our analysis. The Tc_enriched neighborhood was associated with a decreased risk for progression (table S3, hazard ratio = 0.01, 95% confidence interval: 0.0001 to 0.88, covariate-adjusted P value = 0.04). Overall, these results aligned with the known functions of T lymphocytes, especially Tc cells, in immune surveillance and tumor control (36, 37). Conversely, tumor-associated macrophages have been shown to suppress immune activation and promote tumor cell survival and metastasis (38, 39). Our results identified specific spatial cellular neighborhoods that contribute to the risk for cancer progression after surgery.

Identify microenvironmental features predictive of immunotherapy response

We then aimed to identify features of the TME associated with responsiveness to immunotherapy. To this end, we collected tumor samples prior to anti-PD-1/PD-L1 antibody treatment from 34 patients. Patients were categorized as responders ($n = 11$) or nonresponders ($n = 23$) based on radiological assessment and oncologists' evaluation (Materials and Methods and table S4). No significant differences were found in the distribution of gender ($P = 0.44$), cancer stage ($P = 0.23$), histologic classification ($P = 1.00$), or smoking status ($P = 0.16$) between responders and nonresponders (chi-square test). In our mIF imaging analysis (152 cores/22 patients), the average proportion of Tc cells was 2.5 times higher (9.5% versus 3.8%) in tumors from responders compared to nonresponders (Fig. 2A and fig. S5A, $P = 0.005$).

To characterize spatial interaction patterns between different cell types, we derived an "interaction score" using permutation tests (Materials and Methods). The interaction score is bound between -1 and 1, with a higher interaction score between cell_type_A and cell_type_B indicating that cell_type_A interacts more frequently with cell_type_B in the context of all cell types present within the tissue. We found that both Tc and monocytes interacted more frequently with tumor cells in tissues from responders compared to nonresponders (Fig. 2, B to D, LMEM, $P < 0.01$). In contrast, Tc primarily interacted with fibroblasts in tissues from nonresponders, indicating that these cells may act as a physical barrier between Tc and tumor cells (Fig. 2, B and C). Within NSCLC tissue microenvironments, the antitumor immunity of T lymphocytes is induced by antigen-presenting cells, such as Dc, certain subpopulations of macrophages, and monocytes (40, 41). We found that Dc were more likely to interact with Tc spatially in tumors from responders compared to nonresponders (Fig. 2, B to D, LMEM, $P < 0.001$). In addition, the CD163⁻ macrophages also exhibited more frequent interactions with Tc in tumors from responders, although this

interaction did not reach statistical significance ($P = 0.09$). To further characterize the spatial cellular relationships related to immunotherapy response, we carried out spatial distance analysis. The shortest distance between monocytes and Tc was significantly decreased in tumors from responders compared to nonresponders, and the distance between double-negative T (DNT) cells and vascular cells was also decreased in responders (Fig. 2E, LMEM, $P < 0.05$).

We then assigned each cell to a spatial neighborhood based on the neighborhood phenotype we have identified (Fig. 1F). The average proportion of Tc_enriched neighborhoods was 6.5 times higher (7.8% versus 1.2%) in tissues from responders compared to nonresponders (Fig. 2, F and G, and fig. S5A, $P = 0.04$). The proportion for other spatial neighborhoods was not significantly different between responders and nonresponders. We then defined a cytotoxic T lymphocyte (CTL) score using the proportion of cells assigned to the Tc_enriched neighborhood. Because multiple tumor regions were sampled from each patient, we aggregated the CTL scores at the patient level using the mean, median, or maximum value. In our receiver-operating characteristic (ROC) analysis, using the median CTL score achieved the highest area under the curve (AUC) of 0.90 in identifying treatment responders, whereas using the mean and maximum scores achieved an AUC of 0.78 and 0.67, respectively (Fig. 2H and fig. S5B). Regardless of the feature aggregation approach, using the CTL score to identify treatment responders outperformed the use of PD-L1 immunofluorescence signals (AUC = 0.51 to 0.53) (Fig. 2H and fig. S5B). In addition, patients with higher CTL scores demonstrated extended progression-free survival than patients with low proportions (Fig. 2I, log-rank test, $P = 0.04$). These results indicate that both the proportion of Tc cells and their spatial proximity to antigen-presenting cells within TMEs were associated with enhanced responsiveness to immunotherapy.

Signaling regulation of the TME

Within tumor tissues, immune cell activity is coordinated by a complex repertoire of signaling molecules, including secretive factors, antigen-presenting molecules, membrane receptors, and intracellular enzymes (20). These signaling molecules modulate antitumor immunity by affecting the proliferation, differentiation, and cytotoxic effects of immune cells (42). To gain mechanistic insights into immune cell regulation, we first compared protein expression levels across different cell types using mIF images. As expected, tumor cells expressed higher protein expression levels of PD-L1 and Ki67 compared to other cells (fig. S6, A and B). The antigen-presenting molecule HLA-DR was most highly expressed in Dc and CD163⁺ macrophages. IDO1 (indoleamine 2,3-dioxygenase 1), an intracellular enzyme that plays a critical role in regulating immune response to tumor cells, was most highly expressed in Tc, T_{reg}, and Dc. Granzyme B, a serine protease that promotes the apoptosis of tumor cells, was most highly expressed in Tc cells and DNT cells. PAX5, a nuclear transcription factor that promotes the differentiation and proliferation of B cells (43), was highly expressed by B cells.

Next, we compared cell-type-specific protein expression levels in pretreatment tumor tissues between immunotherapy responders and nonresponders. As expected, the PD-L1 expression levels were significantly increased in tumor cells from responders compared to nonresponders (Fig. 3A, $P < 0.0001$). In addition,

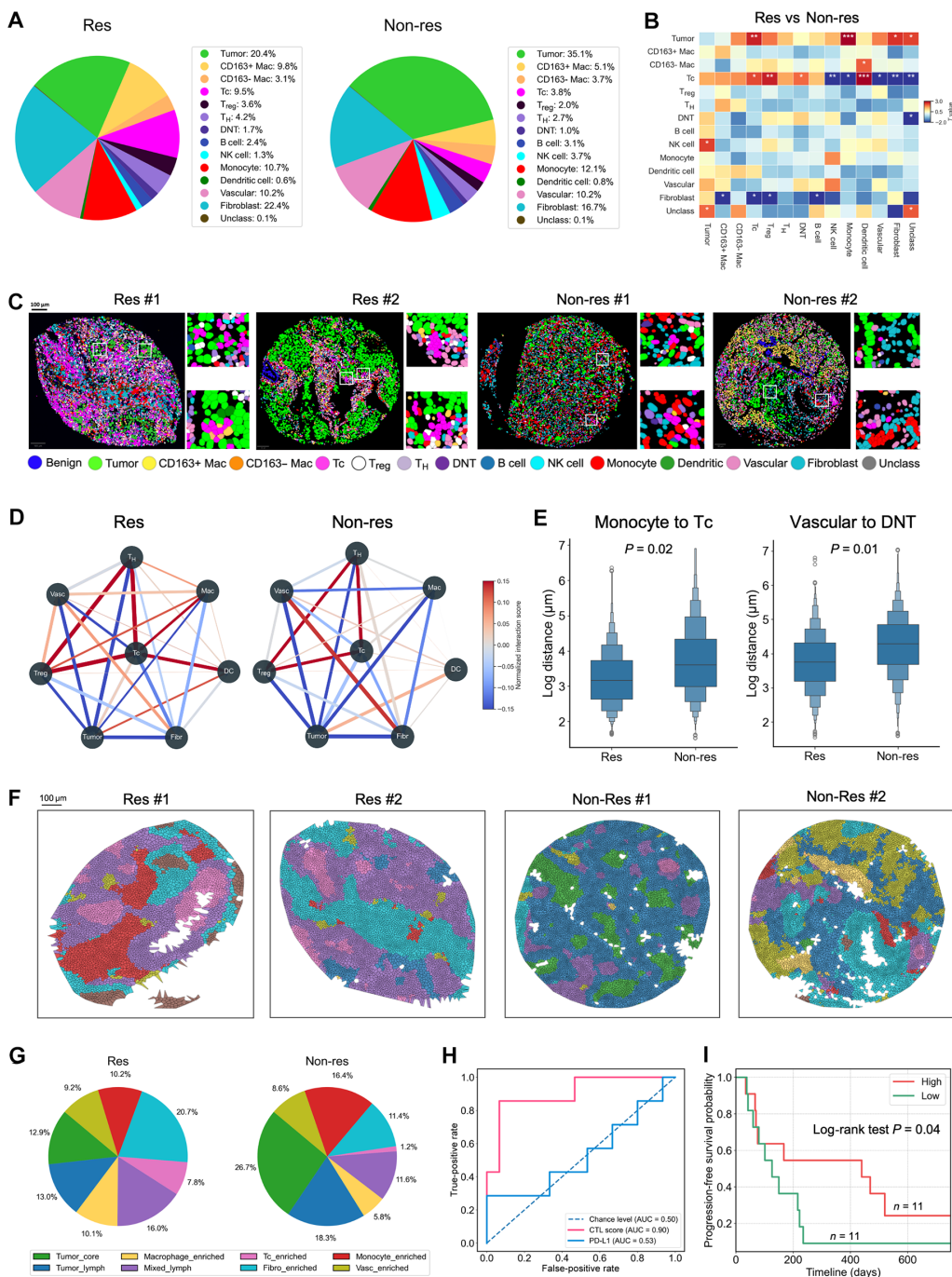


Fig. 2. Identify spatial cellular phenotypes predictive of immunotherapy response. (A) Average cell-type proportions in tumors from responders ($n = 25$ cores/7 patients) and nonresponders ($n = 127$ cores/15 patients). (B) T values comparing cell-type interaction scores between tumors from responders and nonresponders. Red indicates that cell_type_A (x axis) interacts more frequently with cell_type_B (y axis) in responders. T and P values are calculated using an LMEM, with interaction score as the dependent variable, treatment response as a fixed effect, and patients as a random effect. * $P < 0.05$; ** $P < 0.01$; *** $P < 0.001$. (C) Representative tissue core profiles in tumors from responders and nonresponders. (D) Network visualization of the average cell-type (nodes) interaction scores in tumors from responders and nonresponders. Interaction scores (edges) were normalized to a range from -0.15 to 0.15 . (E) Comparing cell-type distance in tumors from responders and nonresponders. P values were calculated using an LMEM, with nucleus centroid distance as the dependent variable, treatment response as a fixed effect, and patients as a random effect. (F) Representative tissue core profiles from responders or nonresponders. Cells are color coded based on neighborhood membership according to (G). (G) Average neighborhood proportions in tumors from responders ($n = 25$ cores/7 patients) and nonresponders ($n = 127$ cores/15 patients). (H) ROC curves showing the performance of the CTL scores and PD-L1 immunofluorescence signals in identifying immunotherapy responders ($n = 22$ patients/7 responders). Scores from multiple cores per patient were aggregated using the median. (I) Kaplan-Meier curves showing the progression-free survival for patients with high or low CTL scores. The cohort is stratified based on the median neighborhood proportion, and survival curves were compared using a one-tailed log-rank test. Mac, macrophage; Tc, cytotoxic T cell; T_{reg}, regulatory T cell; T_H, T helper cell; DNT, double-negative T cell; NK, natural killer cell.

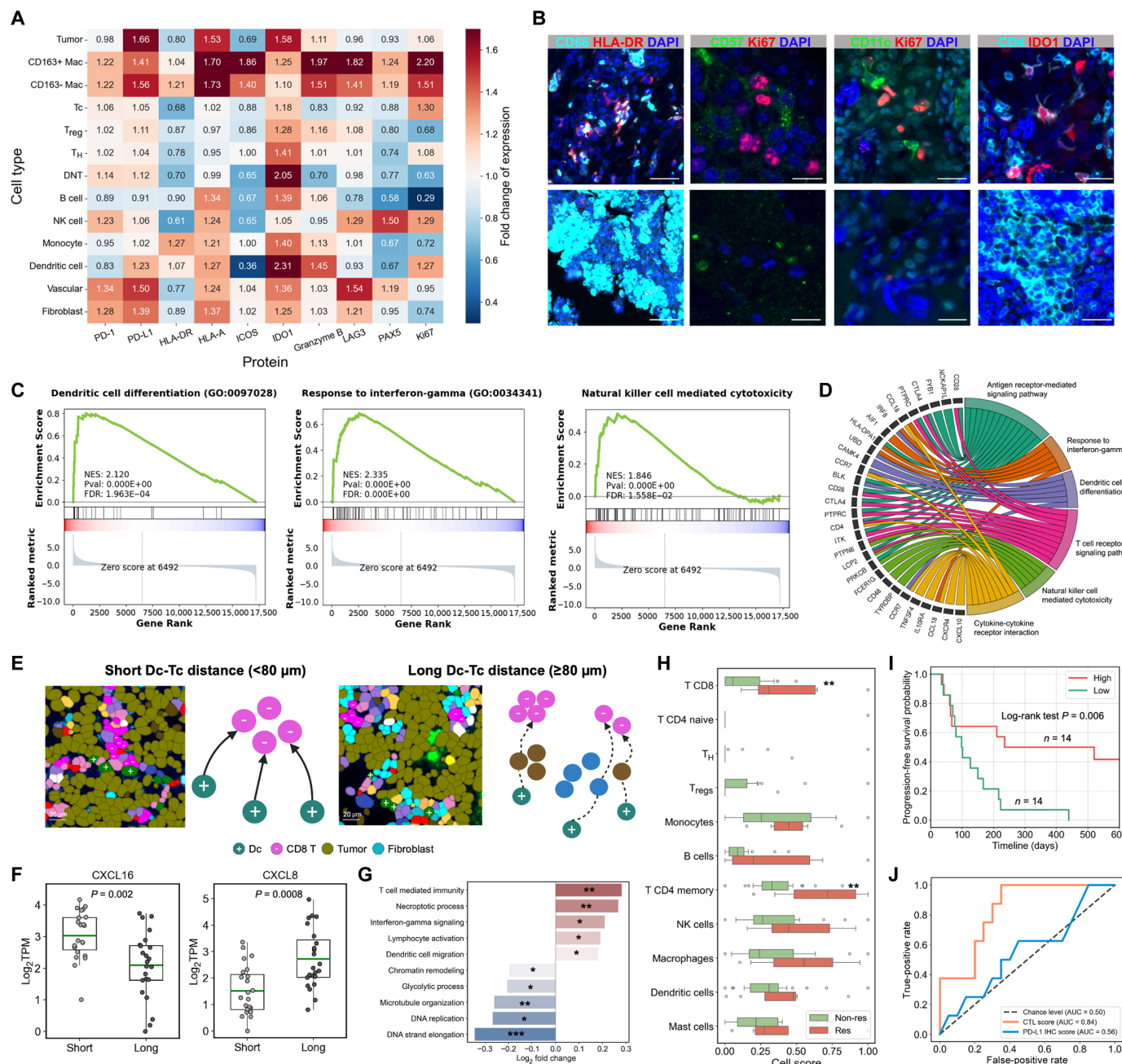


Fig. 3. Enhanced immunoreactive microenvironments in pretreatment tumors from immunotherapy responders compared to nonresponders. (A) Fold change in cell-type-specific protein expression levels in tumors from responders compared to nonresponders. (B) Immunofluorescence signals in tumors from responders (top) and nonresponders (bottom). Scale bars, 50 μ m. (C) GSEA plots showing the overrepresented biological pathways in tumors from responders ($n = 8$) compared to nonresponders ($n = 20$). (D) Circos plot showing the top differentially expressed genes associated with the overrepresented pathways in tumors from responders. (E) Representative tumor regions with short or long spatial distances between Dc and Tc. Distance threshold (80 μ m) was determined by the median value across the entire cohort. (F) Log₂-transformed gene expression values of CXCL16 and CXCL8 in tumors with short or long spatial distance between Dc and Tc ($n = 23$ tissues/23 patients per group). (G) Log₂ fold change of the signaling strength in samples with short Dc-Tc distances compared to those with long distances ($n = 23$ tissues/23 patients per group). P values were calculated using a one-tailed Mann-Whitney U test. * $P < 0.05$; ** $P < 0.01$; *** $P < 0.001$. (H) Cell-type scores inferred from deconvolution analysis of RNA-seq data in tumors from responders ($n = 8$ tissues/8 patients) compared to nonresponders ($n = 22$ tissues/20 patients). For patients with multiple samples, the average score is presented, and P values were calculated using the Mann-Whitney U test. ** $P < 0.01$. (I) Kaplan-Meier curves showing the progression-free survival for patients with high or low CTL scores. The cohort is stratified by the median score, and survival curves were compared using the log-rank test. (J) ROC curves showing the performance of CTL score and PD-L1 IHC scores in identifying immunotherapy responders ($n = 28$ patients/8 responders). Dc, dendritic cells; Tc, cytotoxic T cells.

the average expression levels of HLA-A were increased by 1.7 times in both CD163⁻ and CD163⁺ macrophages from responders, and the expression levels of HLA-DR were also increased, indicating an enhanced antigen-presenting capacity of these cells (Fig. 3, A and B). Published studies have shown that Dc produce interleukins, such as interleukin-12 (IL-12) and IL-15, which enhance the cytotoxicity of natural killer (NK) cells (44). As a positive feedback, NK cells secrete interferon- γ (IFN- γ), CCL5, XCL1, and XCL2, which enhance the antigen presentation and maturation of Dc (45, 46). In our analysis of mIF data, we found that Ki67 expression levels were significantly increased in both Dc and NK cells from responders compared to nonresponders, suggesting enhanced proliferative activity of these cells (Fig. 3, A and B, $P < 0.0001$). Consistent with these results, gene set enrichment analysis (GSEA) of RNA-seq data revealed significant up-regulation of pathways related to Dc differentiation (*IRF8*, *CAMK4*, and *CCR7*), response to IFN- γ (*CCL18*, *UBD*, and *HLA-DPA1*), and NK cell-mediated cytotoxicity (*CD48*, *TYROBP*, and *FCER1G*) in tumors from responders compared to nonresponders (Fig. 3, C and D, and table S5).

In addition to activating NK cells, Dc can enhance the cytotoxic effects of T lymphocytes by recruiting them to tumor sites through cytokine and chemokine signaling (47). Our mIF data analysis has shown that Dc were more likely to spatially interact with Tc in tumors from immunotherapy responders compared to nonresponders (Fig. 2, B to D). Through the analysis of tissue-matched RNA-seq data, we found that the expression levels of chemokine CXCL16 was significantly increased in tumors with shorter spatial distances between Dc and Tc, whereas CXCL6 and CXCL8 expression levels were significantly decreased (Fig. 3, E and F, and fig. S6C). Single-sample GSEA (ssGSEA) demonstrated up-regulation of pathways associated Dc migration, lymphocyte activation, T cell-mediated immunity, and necrotic process in tumors with shorter Dc-Tc distances (Fig. 3G). In contrast, tumors with longer Dc-Tc distances demonstrated up-regulation of pathways related to DNA replication, microtubule organization, chromatin remodeling, and glycolytic process, suggesting enhanced tumor cell proliferation and hypoxic response. In line with these findings, Ki67 protein expression levels were significantly higher in tumor cells within tissues with greater Dc-Tc distances (fig. S6, D and E, $P = 0.04$).

To further characterize immune-related TMEs, we estimated immune cell-type proportions through computational deconvolution of RNA-seq data. The average proportion of CD8 T cells was significantly increased in tissues from responders compared to nonresponders, consistent with our results from the mIF imaging analysis (Fig. 3H, Mann-Whitney U test, $P = 0.006$). In addition, the proportion of CD4 memory T cells was also significantly increased in tissues from responders compared to nonresponders ($P = 0.0096$). In contrast, tissues from nonresponders showed an increased proportion of T_{reg} cells compared to responders, although this increase did not reach statistical significance ($P = 0.31$). We then defined an RNA-seq-based CTL score using the deconvoluted CD8 T cell proportions. Patients with high CTL scores demonstrated significantly better progression-free survival compared to those with low CTL scores (Fig. 3I, log-rank test, $P = 0.006$). Using the CTL score to identify treatment responders achieved an AUC score of 0.84, outperforming the use of PD-L1 IHC score (AUC = 0.56) (Fig. 3J). Collectively, these results suggest that an immunoreactive microenvironment may

predispose patients to a favorable response to immunotherapy prior to treatment initiation.

Develop and validate a deep learning model for cell-type classification using histology images

Although we were able to obtain detailed characterization of TMEs using mIF imaging, generating mIF data remains costly as it demands specialized equipment and trained personnel. In contrast, histology images are collected during routine diagnostics or surgery and are widely available. Compared to mIF data, histology images are more effective at capturing microanatomic features and cellular morphology, offering complementary information by providing a broader context on tissue architecture. Published studies have demonstrated the effectiveness of using deep learning to segment and classify cell nuclei in histology images (48–51). However, many of these deep learning models were trained on human-annotated images, where the accuracy may be negatively affected by the small training datasets and interobserver variabilities.

To address these challenges, we developed NucSegAI, a deep learning model for simultaneous nuclear segmentation and cell-type classification using H&E images. To train NucSegAI, we used a recent dataset of colorectal cancer, which provides mIF images and coregistered H&E-stained histology of the same tissue section (fig. S7A) (52). These two image modalities are spatially aligned at a pixel resolution. Using protein expression markers from mIF images, we classified 2.2 million cells from 10 tissue sections into five categories: tumor ($n = 681,493$), macrophage ($n = 572,758$), lymphocyte ($n = 616,308$), vascular ($n = 164,132$), and fibroblast ($n = 153,555$) (fig. S7B). For evaluation, we trained the model on cells from 80% of the tissue sections, and the remaining 20% were used for validation. In the validation set, the precision, recall, and F1 score for nuclear segmentation performance was 0.78, 0.64, and 0.70, respectively (Fig. 4, A and B). For cell-type classification, the average precision, recall, and F1 score was 0.70, 0.82, and 0.76, respectively. To demonstrate the benefit of training on large-scale, objectively annotated images, we benchmarked our model with the Hover-Net model trained on the CoNSeP dataset (i.e., Hover-CoNSeP) (48). Although the performance for nuclear segmentation was similar between the two models, NucSegAI achieved 2.5 times higher average performance in cell-type classification compared to Hover-CoNSeP (Fig. 4C and fig. S7C).

Given the morphological differences in tumor cells between colorectal cancer and NSCLC, we then fine-tuned the model using a small subset of NSCLC histology images ($n = 30$) annotated with mIF data and pathologist experts, and the fine-tuned model was tested on the remaining held-out images ($n = 150$) (Fig. 4D). To benchmark its predictive performance, we considered two existing models for lung cancer tissue analysis: the HD-Yolo model, trained on proprietarily annotated images from the National Lung Screening Trial (termed Yolo-NLST) (50), and the Hover-Net model, trained on the MoNuSAC dataset (termed Hover-MoNu) (48, 51). It is important to note that, although the Hover-MoNu model recognizes tumor and inflammatory cells (i.e., lymphocytes and macrophages), it does not account for stromal cell types such as fibroblasts or vascular cells, in its predictions (51). In terms of nuclear detection, NucSegAI detected significantly more nucleus for all the considered cell types compared to Yolo-NLST (Fig. 4, E and F, and fig. S7, D and E, Mann-Whitney U test, $P \leq 7.80 \times 10^{-39}$). Although Yolo-NLST captured a limited number of tumor cells, it could

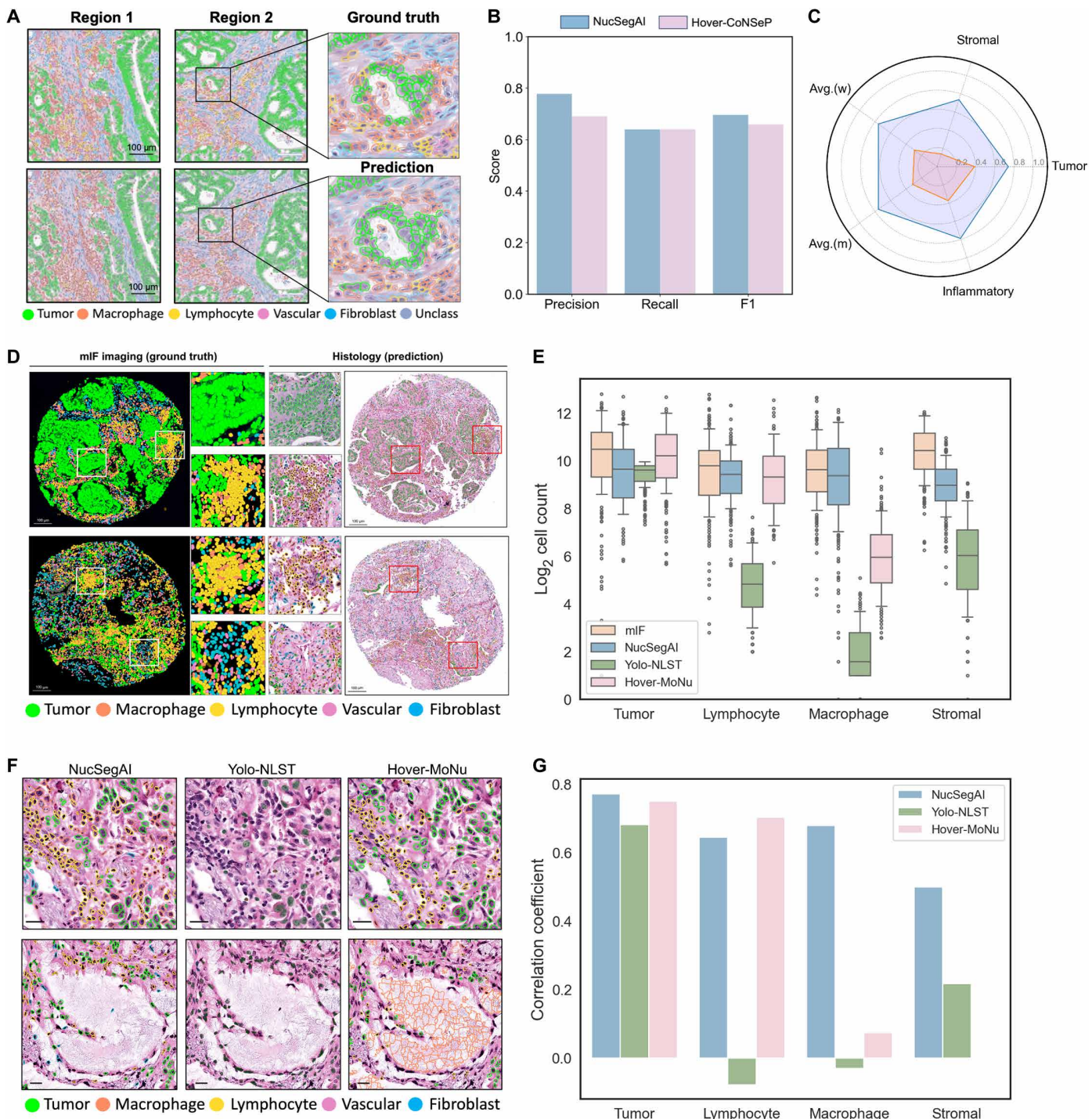


Fig. 4. Development of a deep learning model for automated nucleus segmentation and classification using histology images. (A) Ground truth (top) and predicted (bottom) nuclear types in two example regions of a tumor. Cell nuclei were enclosed by circles and colored by type. (B) Comparison of nuclear segmentation performance between the NucSegAI and the Hover-Net model trained on the CoNSeP dataset. (C) Comparison of cell-type classification performance between the NucSegAI and Hover-CoNSeP models. Macrophages and lymphocytes were combined into the inflammatory class, whereas vascular cells and fibroblasts were combined into the stromal class. F1 scores are presented for each class, along with the micro and weighted averages. (D) Spatial visualization of cell-type distributions in mIF images (left) and those predicted from histology images (right) of two representative TMA cores. Zoomed-in pictures (middle) display regions enclosed by the squares within the main panel. (E) Number of nuclei detected in mIF images and those segmented in paired histology images by different histology-based models ($n = 150$ images). (F) Histology images show nuclear classification results from three histology-based models within two example regions. Scale bars, 20 μm . (G) Spearman correlation coefficients between nuclear types classified from mIF data and those predicted from paired histology images.

not effectively segment inflammatory and stromal cells (Fig. 4F). Compared to the Hover-MoNu model, NucSegAI detected a similar number of tumor cells and lymphocytes but captured significantly more macrophages (Mann-Whitney U test, $P = 3.26 \times 10^{-29}$). In contrast, Hover-MoNu mis-segmented acellular components as macrophages (Fig. 4, F and G). As a result, the average correlation coefficient between the ground truth and predicted numbers of macrophages was 9.2 times higher for NucSegAI compared to Hover-MoNu. These results highlight the superior sensitivity, accuracy, and granularity of NucSegAI in nuclear segmentation and classification.

Histology-based single-cell topological analysis reveals lymphocyte phenotypes predictive of immunotherapy response

To investigate how spatial cellular organization is associated with clinical outcomes within a broader tissue context, we applied NucSegAI to 119 whole-slide histology images from 115 patients with NSCLC treated at Stanford Medical Center (fig. S1 and table S1). In total, we detected 19.7 million tumor cells, 12.3 million lymphocytes, 3.3 million macrophages, 0.7 million vascular cells, and 9.6 million fibroblasts. Because our mIF imaging results have revealed significant associations between lymphocyte phenotypes and immunotherapy response, we focused on the phenotypic analysis of lymphocytes. To dissect the phenotypic diversity of lymphocytes from histology images, we performed single-cell morphological and topological profiling (sc-MTOP) analysis (53). For each cell nucleus, we calculated its features at three different levels: morphological, textural, and topological (Fig. 5A). Morphological features described the nuclear shape and contour, textural features characterized pixel distribution patterns within nuclear contours, and topological features were calculated using a graph-based computational approach (Materials and Methods and table S6). To model spatial relationships between lymphocytes and their microenvironments, we constructed a neighborhood graph between each pair of different cell types. Namely, each lymphocyte appears in five types of neighborhood graphs: lymphocyte-lymphocyte (L-L), lymphocyte-tumor (L-T), lymphocyte-macrophage (L-M), lymphocyte-vascular (L-V), and lymphocyte-fibroblast (L-F) (Fig. 5A). The topological features of a cell were then calculated separately from each type of the graphs it appeared in, and the multilevel features were concatenated to represent its characteristics.

Using unsupervised clustering analysis, we classified lymphocytes into 12 phenotype clusters, namely, Lym0 to Lym11 (Fig. 5, B and C, and fig. S8A). Among these clusters, lymphocytes from Lym0, Lym1, Lym2, Lym5, Lym7, and Lym9 demonstrated a locally aggregated pattern, as characterized by the high L-L Nsubgraph, degrees, coreness, and short L-L edges (Fig. 5C). Lym1 and Lym7 contain lymphocytes spatially connected to tumor cells, and Lym2 and Lym7 were further distinguished by spatial connections to macrophages (Fig. 5, B and C). Lym9 contained lymphocytes spatially connected to fibroblasts, and Lym3 and Lym5 contained lymphocytes spatially connected to vascular cells. By comparing the phenotype proportions of lymphocytes between LUAD and LUSC, we found that the proportions of Lym0 and Lym1 were significantly increased in LUSC compared to LUAD (Fig. 5D and fig. S8, B and C, LMEM, Lym0: $P = 0.02$; Lym1: $P = 0.04$). In addition, both Lym6 and Lym10 proportions were significantly increased in tumors from late-stage cancer (stages III to IV) compared to early-stage cancer (stages I to II), whereas the proportions for Lym7 and Lym11 were significantly

decreased in late-stage cancer (fig. S8B, LMEM, Lym6: $P = 9.68 \times 10^{-5}$; Lym10: $P = 0.04$; Lym7: $P = 0.01$; Lym11: $P = 0.048$). The proportion of Lym4 was significantly decreased in former smokers compared to never smokers ($P = 0.04$).

We next compared the histology-based phenotype proportions of lymphocytes with the immune cell-type proportions estimated from deconvolution of sample-matched tissue-level RNA-seq data ($n = 108$ tissues/107 patients). Both Lym2 and Lym7 were significantly correlated with CD8 T cells (Fig. 5E, Spearman's correlation analysis, Lym2: $P = 0.0002$; Lym7: $P = 0.02$), of which Lym2 was further correlated with the expression levels of genes related to activated CTLs, including *GZMA*, *GZMB*, and *EOMES* (fig. S8D, $P < 0.01$). The proportions of Lym0, Lym1, and Lym7 were positively correlated with T_H cells ($P < 0.05$). In contrast, the proportions of Lym3, Lym4, Lym6, and Lym11 were negatively correlated with CD8 T cells, of which Lym3 was positively associated with monocytes, whereas Lym4 and Lym6 were positively associated with Dc and mast cells, respectively ($P < 0.05$).

To further investigate the association between lymphocyte phenotypes and the signaling environment within tumor tissues, we performed ssGSEA (54). The Lym2 proportion was significantly associated with enrichment scores for lymphocyte activation, T cell-mediated immunity, and B cell receptor signaling (Fig. 5F, Spearman's correlation analysis, $P < 0.001$). In contrast, Lym2 was negatively correlated with gene sets regulating epithelial cell development ($P = 0.003$) and fatty acid metabolism ($P = 0.04$). The association between Lym2 proportions and immunoreactive gene expression profiles was further validated in NSCLC tissues from the The Cancer Genome Atlas (TCGA) cohort (fig. S8E, $n = 400$ samples/369 patients). Moreover, patients with high Lym2 proportions demonstrated significantly prolonged overall survival compared to those with low proportions (Fig. 5G, log-rank test, $P = 0.0001$).

To assess how the histology-defined lymphocyte phenotypes were associated with immunotherapy response, we analyzed phenotype proportions in pretreatment tumor tissues from patients who received immunotherapy in the Stanford cohort ($n = 34$ samples/30 patients). The average proportion of Lym2 was significantly higher in tissues from responders than in nonresponders (Fig. 5H, Mann-Whitney U test, $P = 0.02$). Conversely, the proportion of Lym4 was significantly lower in responders than in nonresponders (Fig. 5H, $P = 0.02$). Given that Lym2 was significantly correlated with CD8 T cell scores and immunoreactive gene expression profiles, we derived a histology-based CTL score based on Lym2 proportions. In ROC analysis, the AUC of the CTL score for identifying treatment responders was 0.78, outperforming the predictive performance of PD-L1 IHC scores (AUC = 0.62) (Fig. 5I).

We have independently used the CTL scores derived from mIF images, RNA-seq data and H&E-stained histology to predict patient's response to immunotherapy. Next, we investigated whether integrating results from these three data modalities can improve predictive performance. To this end, we selected immunotherapy-treated patients ($n = 20$) with all three data modalities available, and the CTL scores independently obtained from each modality were summed to generate a "fusion score" for each patient. In our ROC analysis, the mIF images alone achieved an AUC score of 0.89 in identifying treatment responders, the histology images alone achieved an AUC of 0.82, and the RNA-seq data alone achieved an AUC of 0.90. In comparison, the fusion score achieved

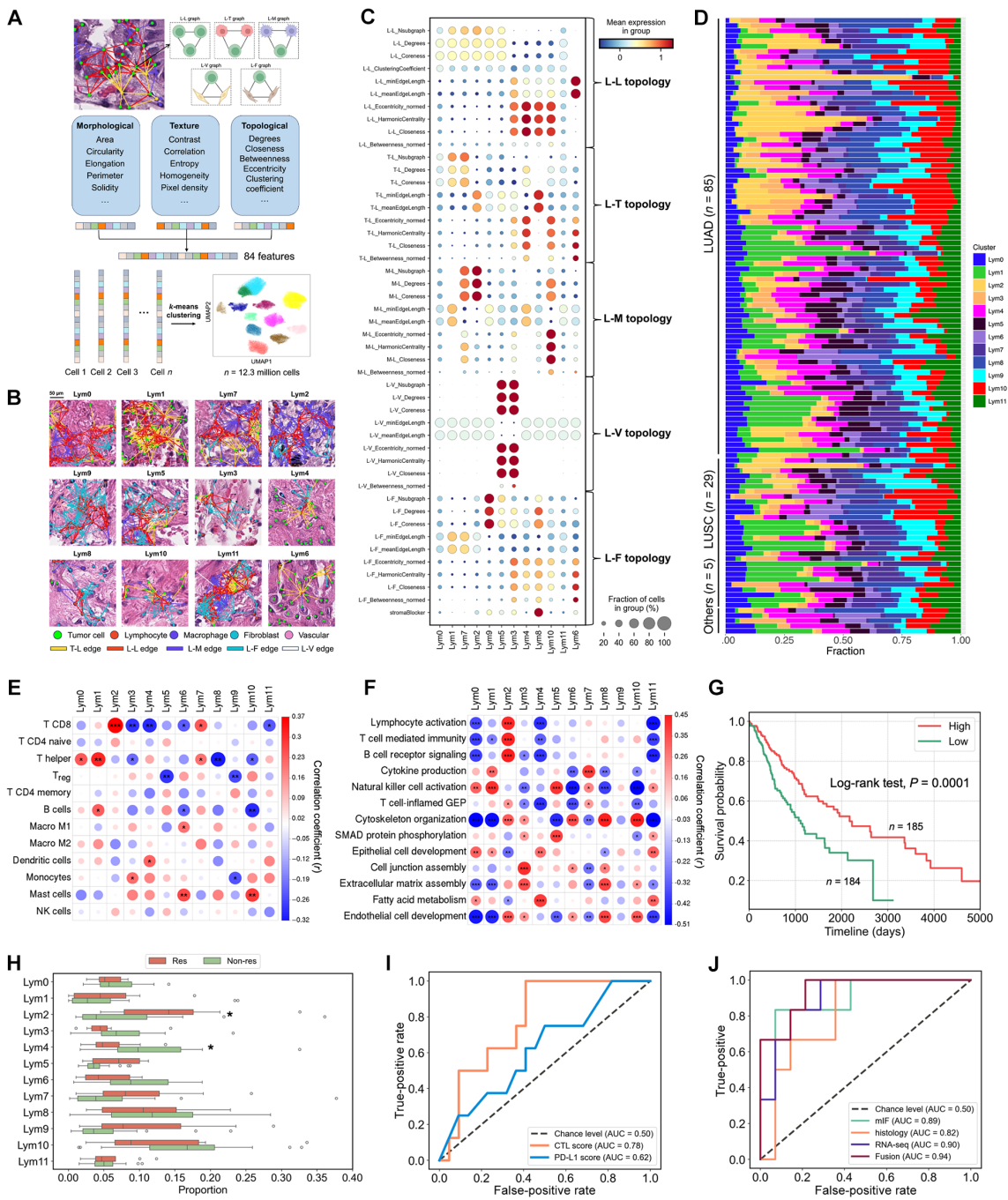


Fig. 5. Identify lymphocyte phenotypes predictive of immunotherapy response from WSIs. (A) Schematic representation of the sc-MTOP analysis. Created in BioRender. Zheng, E. (2025) <https://BioRender.com/hyfdj2h>. (B) Representative spatial cellular graphs for each lymphocyte phenotype. Circles represent nuclear centroids, and lines represent edges connecting spatially adjacent cells. (C) Dot plot showing the values of topological features (y axis) averaged across the lymphocytes belonging to each phenotype (x axis). Color represents z-score normalized values, and size represents the proportion of cells with positive values. (D) Proportions of lymphocyte phenotypes across WSIs. (E and F) Spearman's correlation coefficients between histology-derived lymphocyte phenotype proportions (x axis) and (E) RNA-seq-derived immune cell-type proportions or (F) gene set enrichment scores (y axis) for the same samples. Red indicates a positive correlation, blue indicates a negative correlation, and circle size is proportional to correlation strength ($n = 118$ tissues/107 patients). * $P < 0.05$; ** $P < 0.01$; *** $P < 0.001$. (G) Kaplan-Meier survival curves showing overall survival for patients with high versus low average proportions of Lym2. The cohort is stratified by the median cell proportion ($n = 369$ patients). (H) Phenotype proportions of lymphocytes in tumors from responders ($n = 10$ tissues/8 patients) versus nonresponders ($n = 24$ tissues/22 patients). Box indicates the interquartile range, with the median indicated by the line within the box. When a patient has more than one tissue, the average proportion is shown. P values were determined using the Mann-Whitney U test. * $P < 0.05$. (I) ROC curves showing the performance of CTL scores and PD-1 IHC scores in identifying responders from the immunotherapy-treated cohort ($n = 30$ patients/8 responders). (J) ROC curves illustrate the performance of CTL scores obtained from mIF images, histology images, RNA-seq data, and the fusion of all three modalities in identifying treatment responders ($n = 20$ patients/6 responders).

the highest AUC of 0.94, outperforming any single modality (Fig. 5J). These results indicate that combining microenvironmental modeling data from mIF imaging, RNA-seq, and histology may improve patient stratification.

DISCUSSION

NSCLC is often diagnosed at advanced stage and has a poor prognosis (55). Selecting an effective therapeutic strategy is critical for improving clinical outcomes. In this study, we dissected the cellular heterogeneity and spatial architectures within NSCLC tissues using mIF imaging, whole-slide histology images, and RNA-seq data. We integrated tumor microenvironmental features from these multi-modal datasets using advanced spatial statistical algorithms, and the results led to the identification of spatial cellular relationships predictive of treatment outcomes.

Results from published studies have revealed some associations between the adaptive immune system, formed by T and B lymphocytes, and lung cancer prognosis. In a recent study, Sorin *et al.* characterized the spatial relationships of 1.6 million cells from 416 patients with lung adenocarcinoma using imaging mass cytometry, and the study links B lymphocyte-enriched neighborhoods within tumor tissues to a prolonged overall survival (30). Moreover, the presence of CD4+ Th cells within the B lymphocyte-enriched neighborhood further increases the survival advantage, whereas spatial co-occurrence of T_{reg} cells and B lymphocytes negates the survival advantage (30). Parra *et al.* reported that a higher density of T_{reg} (CD3+CD8-FOXP3+) cells present in tumor tissues are associated with shorter survival in patients with metastatic lung squamous cell carcinoma, whereas a higher density of Tc cells (CD3+CD8+) contributes to an extended survival (56). This result aligned with our observation that higher proportions of Tc cells were associated with a decreased risk for postsurgical progression and enhanced responsiveness to immunotherapy.

Comparing to published studies, our analyses highlighted the associations between innate immune cells and immunotherapy response. Dc are antigen-presenting cells that can activate the adaptive immune response against tumor cells. Recent evidence has revealed the functional impact of Dc in potentiating the clinical benefit of anti-PD1/PD-L1 immunotherapy (47, 57). Our analysis of mIF data revealed significantly higher expression levels of Ki67 in Dc within tumors from immunotherapy responders compared to nonresponders, suggesting enhanced proliferative activity of these cells in responders. Dc have been shown to promote the survival and local expansion of Tc through CXCL16-CXCR6 signaling (58). In our analysis, we demonstrated that Dc were more likely to interact spatially with Tc cells in tumors from immunotherapy responders compared to nonresponders. Integrative analysis with tissue-matched RNA-seq data revealed up-regulation of CXCL16 in tumors where Dc and Tc were in closer proximity. Furthermore, pathways related to Dc migration, IFN- γ signaling, and T cell-mediated immunity were up-regulated in these tumors. In contrast, tumors with greater spatial separation between Dc and Tc showed increased tumor cell proliferation and hypoxia, as indicated by elevated Ki67 expression and up-regulation of DNA replication, chromatin remodeling, and glycolytic pathways. These findings can inform the development of predictive biomarkers to identify patients more likely to respond to immunotherapy and guide the design of therapeutic strategies that enhance immune cell recruitment and spatial organization within the TME.

Although multiplex imaging assays can provide detailed information about TME, they require specialized equipment, reagents, and expertise, making them costly and technically challenging to implement in clinical settings. In contrast, histology images are routinely collected at diagnosis or surgery at no additional cost. Furthermore, the digitization of whole-slide histology images provides high-resolution cellular maps of cancer tissues. However, characterizing TMEs from histology image still represents a challenge. Conventional approaches require IHC on serial tissue sections stained with specific immune cell-type markers. In recent studies, deep learning models have been trained on histology images to aid cell-type annotations. Using human-annotated histology images of lung adenocarcinoma, Rong *et al.* developed HD-Yolo, a deep learning model trained on a lung adenocarcinoma dataset with 12,000 human-annotated cell nuclei (50). To separate spatially overlapping cell nuclei, Graham *et al.* developed Hover-Net, a convolutional neural network using distance map for simultaneous nucleus segmentation and classification (48). The effectiveness of Hover-Net has been tested on multiple image datasets, such as CoNSeP ($n = 24,319$ nuclei) (48) and MoNuSAC ($n = 46,000$ nuclei) (51). Although these models reached publishable performance, their training process was limited by the scarcity of human-annotated datasets. Furthermore, the interobserver variability in nucleus classification may affect their accuracy. Some other existing datasets, such as PanNuke (59), used a semiautomatic approach to label nuclear types. However, the dataset does not contain separate labels for immune cell subsets, such as lymphocytes versus macrophages, but it combined them into a single “inflammatory cell” class. This leads to insufficient granularity for detailed characterization of TME.

To address this challenge, recent spatial multiomics technologies have enabled the coprofiling of molecular features and H&E-stained histology images from the same or adjacent tissue sections, creating new opportunities for integrating molecular profiles with histological features. Jaume *et al.* introduced HEST-1 K, a data repository containing paired spatial transcriptomic profiles and H&E images from 153 public and internal cohorts (60). Wu *et al.* demonstrated the effectiveness of using cell morphological features to computationally infer protein expression levels (61, 62). Andani *et al.* developed HistoPlexer, a deep learning framework that generates spatially resolved protein multiplexes from histopathology images (63). In addition, recently developed histology foundation models, trained on large-scale image or image-text datasets, have shown promising results in downstream tasks such as tumor subtype classification, molecular phenotype prediction, and text-image alignment. In this study, we developed NucSegAI, a deep learning model trained on mIF data and coregistered H&E-stained histology images of the same tissue section. The nucleus types of 2.2 million cells were determined by lineage marker expression, avoiding any human bias and substantially increasing the number of training instances. By benchmarking our deep learning model with existing models, we demonstrated that it advances in granularity, sensitivity, and accuracy. Future work will evaluate the model’s generalizability across additional cancer types beyond NSCLC.

With the advancement of deep learning methods, many studies have used histology images to predict the cancer treatment outcome. These studies can be classified into two broad categories. Some studies predict biomarker status related to treatment response, such as tumor mutation burden (64), microsatellite instability (65, 66), and PD-L1 status (67), whereas some other studies predicting treatment

response directly from histology images (68–70). Because a WSI can contain millions of pixels, conventional analytic approaches involve cropping images into smaller patches, which are then used to train deep learning models. However, a patch can contain from tens to hundreds of cells, potentially limiting the ability to capture the complex spatial relationships between individual cells. In this study, we analyzed WSIs of NSCLC at a single-cell resolution. By characterizing the topological phenotypes of 45.6 million cells across 119 WSIs, we identified specific lymphocyte phenotypes predictive of immunotherapy response. The proportion of Lym2 was strongly correlated with Tc cells and gene expression signatures associated with favorable immunotherapy response. Using histology-defined lymphocyte phenotypes achieved an AUC score of 0.78 in identifying treatment responders, outperforming the conventional PD-L1 IHC score. Our methods offer an automated and scalable approach to characterizing clinically relevant spatial cellular phenotypes from histology images.

Data across different modalities offer complementary insights into tumor microenvironmental features. Multiplex imaging provides detailed characterization of spatial cellular organization at the locoregional level. Comparatively, RNA-seq data captures signaling activation patterns and transcriptomic profiles at the tissue level, whereas whole-slide histology images offer a broader view on cell morphology and topological features. Our findings demonstrate that integrating the unique strengths of each modality through multimodal data analysis enhances the accuracy of therapeutic response prediction compared to relying on a single data modality alone.

In conclusion, this study leverages multimodal datasets to provide a comprehensive characterization of cell-type diversity, spatial cellular relationships, and the signaling environment in NSCLC tissues. We identified clinically relevant TME features associated with cancer progression. Developing effective computational methods to integrate microenvironmental data from multimodal, multiomics biomedical datasets can guide the selection of personalized therapeutic approaches for individual patients, with the potential to improve precision medicine and cancer treatment strategies.

MATERIALS AND METHODS

Experimental design

A cohort of 132 patients with NSCLC was included in this study, which was approved by Stanford's Institutional Review Board (IRB) (#48496). The requirement for informed consent was waived by the IRB due to the deidentified retrospective nature of the study. Clinical characteristics are summarized in table S1. The median age at diagnosis was 70.4 (interquartile range: 65.0 to 76.3). The median follow-up time after diagnosis was 3.6 years, with an interquartile range between 796 and 1876 days. Approximately 57.6% patients were female, and 42.4% were male. Among these patients, 34 (25.8%) received ICI-based immunotherapy, with 24 received pembrolizumab, 8 received durvalumab, and the remaining 2 received nivolumab and atezolizumab, respectively. Treatment response was determined by radiological evidence and evaluations from clinical oncologists using the RECIST 1.1 criteria (71). Patients who developed progressive disease within 12 months after the first treatment were classified as nonresponders, whereas those demonstrating partial/complete response or stable disease for over 12 months were classified as responders (7, 8).

Tissue preprocessing and mIF imaging

Formalin-fixed paraffin-embedded (FFPE) tumor tissues collected from diagnosis or surgery were used to create TMAs. Board-certified pathologists examined the H&E-stained slides, selecting at least two representative central tumor regions as areas of interest. Cylindrical tissue cores with a diameter of 1 mm were extracted from the selected regions using a TMA puncher and then arranged into a recipient paraffin block. Tissues were sectioned from the TMA at 5 μm thickness and mounted onto super adhesive slides. FFPE tissue sections were dewaxed and rehydrated following standard histology methods. mIF imaging was performed with the PhenoCycler-Fusion platform (formerly CODEX) following the standard protocol (Akoya Biosciences, CA, USA) (26). Epitope retrieval was performed using Tris-EDTA (pH 9) for 20 min in a programmable pressure cooker (Instant PotTM). After allowing the pressure cooker to cool and depressurize naturally, the tissue was bleached by immersion in a solution of 4.5% (w/v) H_2O_2 and 20 mM NaOH in phosphate-buffered saline under bright white light-emitting diode light. The tissue section was then stained with a mixture of oligonucleotide barcoded PhenoCycler antibodies listed in table S2 and postfixed according to the user manual. Human tonsil tissues were used as a staining control. The tissue was then imaged at a resolution of 0.5 μm / pixel. Before imaging, a reporter plate with up to three complementary oligonucleotide-fluorophore reporters per cycle was prepared according to the user manual. Signal specificity was assessed by visual inspection.

Cell segmentation and classification on mIF images

mIF images were imported into the QuPath software (version 0.4.2) in the qptiff format. We applied a Gaussian blur filter with a radius of 2.5 to the DAPI (4',6-diamidino-2-phenylindole) channel and segmented cells using a pretrained StarDist model (version 0.4.0) (72). The quality of cell segmentation was assessed through visual inspection of paired histology images, and incorrectly segmented cells were manually corrected through the graph interface within QuPath. A hierarchical lineage assignment strategy was used for cell-type classification (30). Starting from the root node of a hierarchical tree, cells were categorized into a positive or negative class based on the expression levels of a specific protein marker, where the threshold was determined using a Gaussian mixture model (GMM). The PanCK+ cells were further classified into benign or malignant cells based on board-certified pathologist (M.O. and B.E.H.) annotation. Cell features, such as two-dimensional (2D) coordinate, protein expression levels, and classified type, were exported into a csv file, with each row representing a cell and columns indicating the feature values.

Spatial cellular interaction analysis

From the cell segmentation, we obtained 2D geometric coordinates for the centroid of each cell nucleus. These centroids form a discrete point set on a 2D plane. Cells within TMEs are known to communicate with each other through paracrine, autocrine, and/or juxtacrine mechanisms. For each cell, we used the radius-based neighbor learning approach implemented by the sklearn library (version 1.5) to identify its neighbors. The radius of a neighborhood was set to 50 μm . To quantify spatial cellular interactions, we consider two metrics: the frequency of spatial connections and the absolute Euclidean distance. The frequency of spatial connections is directional, indicating the likelihood of one cell type being spatially interacted

with another cell type. The frequency was calculated using a permutation test. Specifically, for each query cell, we permuted its neighborhood cell types 1000 times using all cell types present within a tissue core. Thus, the “interaction score” derived from our permutation analysis represents the observed frequency of spatial adjacency between two cell types compared to a random distribution within the tissue context.

Identification of recurrent spatial neighborhood phenotype

To identify recurrent neighborhood phenotypes that share similar spatial cell distribution patterns across tissues, we first determined the neighborhood of each cell using the radius-based neighbor learning approach described above. For each cell, we counted the number of cells belonging to each phenotype within its neighborhood, resulting in a matrix with dimensions $n_{\text{cells}} \times n_{\text{cell_types}}$. We then performed unsupervised clustering analysis on this matrix using k -means. The optimal number of clusters (K) was determined using Calinski-Harabasz and Davies-Bouldin indices.

Training the Hover-Net model for nuclear segmentation and classification on histology images

Dataset description

We downloaded a publicly available multimodal image dataset of colorectal cancer (52). The dataset contains mIF images and coregistered whole-slide histology images of the same tissue section. The two image modalities have been spatially aligned at a pixel resolution (52). Because a WSI typically contained millions of cells, we randomly selected 10 WSIs based on subsequent analyses: CRC02, CRC03, CRC04, CRC06, CRC08, CRC14, CRC17, CRC23, CRC26, and CRC38.

Cell-type classification and data preparation

Cell types were classified based on protein expression levels using a similar hierarchical lineage assignment strategy as described for our mIF analyses. Cells were partitioned into a positive class, or a negative class, based on the expression level of each specific protein marker, where the threshold was determined by the GMM. To train the Hover-Net model, we cropped WSIs into $500 \mu\text{m} \times 500 \mu\text{m}$ patches. Because our primary goal is to profile immune-related microenvironments, we removed the tumor regions with low density of immune cells. Specifically, we selected the patches based on two criteria: (i) the number of cells present in a patch should be greater than 200, which helped to remove the imaging background, and (ii) the immune cell fraction, calculated as the sum of the fraction of lymphocytes and macrophages, should be greater than 0.3. Because samples prepared in different batches differ in colors, we performed stain normalization using StainTools (version 2.1.2, <https://github.com/Peter554/StainTools>). For this purpose, we used one representative slide from the Stanford cohort as the reference and normalized the color of the other images to match the reference.

Training and evaluation

The Hover-Net model architecture has been previously described (48). Briefly, the model consists of tandem convolution units, residual units, and decoder units. These units form three branches: (i) the nuclear pixel branch, (ii) the Hover branch, and (iii) the nuclear classification branch, enabling simultaneous nuclear segmentation and classification. We used a transfer learning approach, where the model was initiated with the pretrained weights on the PanNuke dataset (59) and was then fine-tuned on the colorectal dataset. Following the standard two-stage training scheme of Hover-Net, we

first trained the decoder unit for 10 epochs while freezing the weights of the other layers. In the second stage, we trained all layers for another 10 epochs. The model was optimized using the Adam optimizer with a learning rate set to 0.0001. To classify cell types in NSCLC tissues, the model was fine-tuned for an additional 10 epochs using NSCLC images annotated with paired mIF data and expert pathologists ($n = 30$ images, 206,160 nuclei).

For evaluation, Hover-Net generated class predictions for each nuclear pixel, and the class of a nucleus was assigned based on the majority class of all its pixels. We used precision, recall, and F1 score to assess the performance for nuclear segmentation and cell-type classification.

Benchmark with existing models

We benchmarked the performance of NucSegAI with three existing models: (i) Hover-Net model pretrained on the CoNSeP dataset (Hover-CoNSeP) (48), (ii) Hover-Net model pretrained on the MoNuSAC dataset (Hover-MoNu) (51), and (iii) HD-Yolo model pretrained on lung cancer histopathological images from the National Lung Screening Trial (50). For benchmarking with Hover-CoNSeP, we followed the cell-type annotation scheme from the original study (48), where macrophages and lymphocytes were grouped into an inflammatory class, and fibroblast and vascular cells were combined into a stromal class.

Single-cell morphological and topological analysis

Feature extraction

Hover-Net outputs the nuclear centroid and contour for each cell on the WSI. Morphological, textural, and topological features were then calculated from each cell, following previously described methods (53). A detailed description of each feature can be in table S6. Morphological features were calculated based on the nuclear shape and contour, whereas textural features were calculated based on pixel distribution patterns within the nuclear contour. Topological features characterize the intercellular spatial relationship at a single-cell resolution, calculated using a graph-based approach. For each cell, we constructed a spatial neighborhood graph. Within the graph, vertices represent nuclear centroids and edges were configured using the k -nearest neighbor algorithm. A cell is connected to its five nearest neighbors, and edges longer than a threshold of $25 \mu\text{m}$ were removed.

This study focused on the analysis of tumor cells. To comprehensively describe intercellular relationships between tumor cells and the microenvironment cells, a neighborhood graph was constructed between each different pair of cell types. Namely, a lymphocyte appears in five types of graphs: lymphocyte-lymphocyte graph (Graph_L-L), lymphocyte-tumor graph (Graph_L-T), lymphocyte-macrophage graph (Graph_L-M), lymphocyte-vascular graph (Graph_L-V), and lymphocyte-fibroblast graph (Graph_L-F). For each cell, the topological features were calculated from each type of graph separately, and features obtained from all types of graphs were concatenated for downstream analysis.

Identification of cells with similar characteristics

The output from the sc-MTOP analysis was a matrix of dimension $(N_{\text{cell_number}}, D_{\text{feature}})$, where N represents the number of cells in a WSI, and D_{feature} represents the length of a feature vector ($D_{\text{feature}} = 84$). To identify tumor cells of similar characteristics, we performed k -means clustering analysis. To train a k -means classifier, we randomly subset 20% of cells from each WSI. Feature values were log transformed, and each feature was scaled to unit variance and zero

mean across all selected cells. We applied $k = 12$ based on a balanced consideration of granularity and interpretability. To calculate the phenotype proportions of the cells in the entire WSI, we applied the trained k -means classifier to the feature matrix of all cells.

Validation of the sc-MTOP model on independent datasets

To validate the association between histology-defined lymphocyte phenotypes and clinically relevant signaling microenvironments, we used paired WSIs and RNA-seq data from the TCGA-LUAD and TCGA-LUSC cohorts (73, 74). Data were retrieved from the publicly available TCGA archive (<https://portal.gdc.cancer.gov>). Given that a single WSI typically contains millions of cells, profiling tissue microenvironments at a single-cell resolution is computationally expensive. To address this, we selected 400 WSIs from 369 patients based on RNA-seq profiles. Specifically, we performed ssGSEA using RNA-seq data from the entire cohort (1046 WSIs from 949 patients) as previously described (75). For each sample, we calculated the enrichment score for immunoreactive gene ontological pathways, including lymphocyte activation (GO:0051251), T cell-mediated immunity (GO:0002456), B cell receptor signaling pathway (GO:0050853), and NK cell activation (GO:0030101). The enrichment score for each pathway was min-max normalized across the entire cohort and then averaged to generate an “immunoreactive score.” We then ranked the samples based on their respective immunoreactive scores and selected the top 100 samples with the highest and lowest scores from the LUAD and LUSC cohort, respectively.

Each WSI was cropped into nonoverlapping patches of 4000 by 4000 pixels (1000 μm by 1000 μm), and we selected the top 5 patches with the highest tissue coverage, based on the ratio of tissue foreground to background. NucSegAI was then applied to each patch, and nucleus features were calculated as described above. Each feature was scaled using the mean and SD obtained from the Stanford training set, and the same k -means classifier trained on the Stanford cohort was used to detect nucleus phenotypes. The phenotype counts from individual patches were summed to represent the entire slide.

Tissue-level RNA-seq and computational deconvolution

To generate transcriptomics profiles at the tissue level, we performed FFPE RNA-seq. Total RNA was isolated using the Promega Maxwell RSC RNA FFPE Kit (catalog no. AS1440), and the quality and quantity were measured using the Tapestation 4200 (Agilent Technologies) and Qubit (Invitrogen), respectively. For library preparation, the Takara SMARTer Stranded Total RNA-Seq Kit v2-Pico Input Mammalian kit (catalog no. 634414) was used following the manufacturer’s instructions. cDNA fragments were synthesized from 10 ng of total RNA using random primers. SMART technology was used to preserve the strand orientation information. Adapters for Illumina sequencing (with specific barcodes) was added through polymerase chain reaction using five cycles. The ribosomal cDNA fragments were then cleaved using the ZapR v2 enzyme in the presence of ribosomal RNA (rRNA)-specific probes. The library fragments from non-rRNA molecules were then enriched by a second round of amplification. The final library quality was estimated using the Agilent Tapestation 4200 and quantification by Qubit Flex (Invitrogen). Before sequencing, libraries were diluted to 4 nmol and pooled. Pooled libraries were loaded on the NovaSeq 6000 (Illumina) for paired-end sequencing following the manufacturer’s instructions. Raw reads were generated from run BCL files using the tool bcl2fastq v2.20.0.422. Quality control of the reads was assessed

using in-house fastqc scripts. Most of the samples showed 90% of reads $Q > 30$. Sequencing reads were aligned to the human transcriptome, and transcripts were quantified using Salmon (version 1.10.2) (76). We used the CIBERSORTx algorithm to estimate immune cell-type proportions from RNA-seq data (77), using the LM22 dataset as reference gene expression matrix (77). The cell-type scores inferred from RNA-seq data were min-max normalized across the immunotherapy-treated cohort.

Gene set enrichment analysis

Differential gene expression analysis was performed using DESeq2 (78). Genes were ranked by $\text{Sign}(\log_2 \text{FC}) \times -\log P$, where FC represents the fold change, and P represents the P value obtained from the differential gene expression analysis. Biological processes were obtained from Gene Ontology, and molecular pathways were collected from the Kyoto Encyclopedia of Genes and Genomes database. GSEA was performed using the GSEAPy package (version 1.1) (79).

Statistical analysis

All statistical analyses were performed in Python (version 3.10). No statistical methods were used to predetermine the sample size. Pairwise comparisons were conducted using two-tailed Mann-Whitney U tests, unless otherwise specified in the figure legends, with the statsmodels module (version 0.14.4). Correlation analyses were carried out using the Spearman’s correlation method, as specified in the figure legends. For analyses involving multiple cores or tissue regions per patient, an LMEM was applied, incorporating patient IDs as a random effect, with P values obtained from the Wald test. Tumors from current or daily smokers, as well as those classified under “Other” in histologic classification, were excluded from the comparison due to their small sample size.

Survival analyses were performed using the lifelines package (version 0.30.0). Measurements from multiple tissue regions per patient were aggregated using the mean, median, or maximum value, as specified in the figure legends. Kaplan-Meier analysis was used to compare survival outcomes between patient groups, with P values calculated using the log-rank test. To adjust for clinical variables, Cox regression analysis was performed.

Supplementary Materials

The PDF file includes:

Figs. S1 to S8

Legends for tables S1 to S6

Other Supplementary Material for this manuscript includes the following:

Tables S1 to S6

REFERENCES AND NOTES

1. M. G. Oser, M. J. Niederst, L. V. Sequist, J. A. Engelman, Transformation from non-small-cell lung cancer to small-cell lung cancer: Molecular drivers and cells of origin. *Lancet Oncol.* **16**, e165–e172 (2015).
2. R. Arriagada, B. Bergman, A. Dunant, T. Le Chevalier, J.-P. Pignon, J. Vansteenkiste, International Adjuvant Lung Cancer Trial Collaborative Group, Cisplatin-based adjuvant chemotherapy in patients with completely resected non-small-cell lung cancer. *N. Engl. J. Med.* **350**, 351–360 (2004).
3. K. al-Kattan, E. Sepsas, S. W. Fountain, E. R. Townsend, Disease recurrence after resection for stage I lung cancer. *Eur. J. Cardiothorac. Surg.* **12**, 380–384 (1997).
4. W. M. Alberts, Follow up and surveillance of the patient with lung cancer: What do you do after surgery? *Respirology* **12**, 16–21 (2007).
5. F. B. Zimmermann, M. Molls, B. Jeremic, Treatment of recurrent disease in lung cancer. *Semin. Surg. Oncol.* **21**, 122–127 (2003).

6. A. Chang, Chemotherapy, chemoresistance and the changing treatment landscape for NSCLC. *Lung Cancer* **71**, 3–10 (2011).
7. M. Reck, D. Rodriguez-Abreu, A. G. Robinson, R. Hui, T. Csöszai, A. Fülop, M. Gottfried, N. Peled, A. Tafreshi, S. Cuffe, M. O'Brien, S. Rao, K. Hotta, M. A. Leiby, G. M. Lubiniecki, Y. Shentu, R. Rangwala, J. R. Brahmer, Pembrolizumab versus chemotherapy for PD-L1-positive non-small-cell lung cancer. *N. Engl. J. Med.* **375**, 1823–1833 (2016).
8. H. Borghaei, L. Paz-Ares, L. Horn, D. R. Spigel, M. Steins, N. E. Ready, L. Q. Chow, E. E. Vokes, E. Felip, E. Holgado, F. Barlesi, M. Kohlhäufel, O. Arrieta, M. A. Burgio, J. Fayette, H. Lena, E. Poddubskaya, D. E. Gerber, S. N. Gettinger, C. M. Rudin, N. Rizvi, L. Crino, G. R. Blumenschein Jr., S. J. Antonia, C. Dorange, C. T. Harbison, F. Graf Finckenstein, J. R. Brahmer, Nivolumab versus docetaxel in advanced nonsquamous non-small-cell lung cancer. *N. Engl. J. Med.* **373**, 1627–1639 (2015).
9. J. Brahmer, K. L. Reckamp, P. Baas, L. Crino, W. E. Eberhardt, E. Poddubskaya, S. Antonia, A. Pluzanski, E. E. Vokes, E. Holgado, D. Waterhouse, N. Ready, J. Gainor, O. Arén Frontera, L. Havel, M. Steins, M. C. Garassino, J. G. Aerts, M. Domine, L. Paz-Ares, M. Reck, C. Baudelot, C. T. Harbison, B. Lestini, D. R. Spigel, Nivolumab versus docetaxel in advanced squamous-cell non-small-cell lung cancer. *N. Engl. J. Med.* **373**, 123–135 (2015).
10. E. B. Garon, N. A. Rizvi, R. Hui, N. Leighl, A. S. Balmanoukian, J. P. Eder, A. Patnaik, C. Aggarwal, M. Gubens, L. Horn, E. Carcereny, M.-J. Ahn, E. Felip, J.-S. Lee, M. D. Hellmann, O. Hamid, J. W. Goldman, J.-C. Soria, M. Dolled-Filhart, R. Z. Rutledge, J. Zhang, J. K. Lunceford, R. Rangwala, G. M. Lubiniecki, C. Roach, K. Emancipator, L. Gandhi, Pembrolizumab for the treatment of non-small-cell lung cancer. *N. Engl. J. Med.* **372**, 2018–2028 (2015).
11. M. J. Grant, R. S. Herbst, S. B. Goldberg, Selecting the optimal immunotherapy regimen in driver-negative metastatic NSCLC. *Nat. Rev. Clin. Oncol.* **18**, 625–644 (2021).
12. M. Reck, D. Rodríguez-Abreu, A. G. Robinson, R. Hui, T. Csöszai, A. Fülop, M. Gottfried, N. Peled, A. Tafreshi, S. Cuffe, M. O'Brien, S. Rao, K. Hotta, T. A. Leal, J. W. Riess, E. Jensen, B. Zhao, M. C. Pietanza, J. R. Brahmer, Five-year outcomes with pembrolizumab versus chemotherapy for metastatic non-small-cell lung cancer with PD-L1 tumor proportion score ≥ 50%. *J. Clin. Oncol.* **39**, 2339–2349 (2021).
13. B. C. Cho, Y. Wu, G. Lopes, I. Kudaba, D. M. Kowalski, H. Z. Turna, G. De Castro Jr, C. Caglevic, L. Zhang, B. Karaszewska, K. K. Laktionov, V. Srimuninnimit, I. Bondarenko, K. Kubota, L. Yin, J. Lin, F. Souza, T. S. K. Mok, FP13.04 KEYNOTE-042 3-year survival update: 1L pembrolizumab vs platinum-based chemotherapy for PD-L1+ locally advanced/metastatic NSCLC. *J. Thorac. Oncol.* **16**, S225–S226 (2021).
14. G. Lopes, Y.-L. Wu, I. Kudaba, D. Kowalski, B. C. Cho, G. Castro, V. Srimuninnimit, I. Bondarenko, K. Kubota, G. M. Lubiniecki, J. Zhang, D. A. Kush, T. Mok, Pembrolizumab (pembro) versus platinum-based chemotherapy (chemo) as first-line therapy for advanced/metastatic NSCLC with a PD-L1 tumor proportion score (TPS) ≥ 1%: Open-label, phase 3 KEYNOTE-042 study. *J. Clin. Oncol.* **36**, LBA4-LBA4 (2018).
15. D. L. Rimm, G. Han, J. M. Taube, E. S. Yi, J. A. Bridge, D. B. Flieder, R. Homer, W. W. West, H. Wu, A. C. Roden, J. Fujimoto, H. Yu, R. Anders, A. Kowalewski, C. Rivard, J. Rehman, C. Batenchuk, V. Burns, F. R. Hirsch, I. I. Wistuba, A prospective, multi-institutional, pathologist-based assessment of 4 immunohistochemistry assays for PD-L1 expression in non-small cell lung cancer. *JAMA Oncol.* **3**, 1051–1058 (2017).
16. N. Ready, M. D. Hellmann, M. M. Awad, G. A. Otterson, M. Gutierrez, J. F. Gainor, H. Borghaei, J. Jolivet, L. Horn, M. Mates, J. Brahmer, I. Rabinowitz, P. S. Reddy, J. Chesney, J. Orcutt, D. R. Spigel, M. Reck, K. J. O'Byrne, L. Paz-Ares, W. Hu, K. Zerba, X. Li, B. Lestini, W. J. Geese, J. D. Szustakowski, G. Green, H. Chang, S. S. Ramalingam, First-line nivolumab plus ipilimumab in advanced non-small-cell lung cancer (CheckMate 568): Outcomes by programmed death ligand 1 and tumor mutational burden as biomarkers. *J. Clin. Oncol.* **37**, 992–1000 (2019).
17. D. T. Le, J. N. Uram, H. Wang, B. R. Bartlett, H. Kemberling, A. D. Eyring, A. D. Skora, B. S. Luber, N. S. Azad, D. Laheru, B. Biedrzycki, R. C. Donehower, A. Zaheer, G. A. Fisher, T. S. Crocenzi, J. J. Lee, S. M. Duffy, R. M. Goldberg, A. de la Chapelle, M. Koshiji, F. Bhajee, T. Huebner, R. H. Hruban, L. D. Wood, N. Cuka, D. M. Pardoll, N. Papadopoulos, K. W. Kinzler, S. Zhou, T. C. Cornish, J. M. Taube, R. A. Anders, J. R. Eshleman, B. Vogelstein, L. A. Diaz Jr., PD-1 blockade in tumors with mismatch-repair deficiency. *N. Engl. J. Med.* **372**, 2509–2520 (2015).
18. A. Rittmeyer, F. Barlesi, D. Waterkamp, K. Park, F. Ciardiello, J. von Pawel, S. M. Gadgil, T. Hida, D. M. Kowalski, M. C. Dols, D. L. Cortinovis, J. Leach, J. Polikoff, C. Barrios, F. Kabbinavar, O. A. Frontera, F. De Marinis, H. Turna, J.-S. Lee, M. Ballinger, M. Kowanetz, P. He, D. S. Chen, A. Sandler, D. R. Gandara, OAK Study Group, Atezolizumab versus docetaxel in patients with previously treated non-small-cell lung cancer (OAK): A phase 3, open-label, multicentre randomised controlled trial. *Lancet* **389**, 255–265 (2017).
19. W. A. Cooper, P. A. Russell, M. Cherian, E. E. Duhig, D. Godbolt, P. J. Jessup, C. Khoo, C. Leslie, A. Maher, D. F. Moffat, V. Sivasubramaniam, C. Faure, A. Reznichenko, A. Grattan, S. B. Fox, Intra- and interobserver reproducibility assessment of PD-L1 biomarker in non-small cell lung cancer. *Clin. Cancer Res.* **23**, 4569–4577 (2017).
20. N. K. Altorki, G. J. Markowitz, D. Gao, J. L. Port, A. Saxena, B. Stiles, T. McGraw, V. Mittal, The lung microenvironment: An important regulator of tumour growth and metastasis. *Nat. Rev. Cancer* **19**, 9–31 (2019).
21. Y. Zheng, F. Carrillo-Perez, M. Pizurica, D. H. Heiland, O. Gevaert, Spatial cellular architecture predicts prognosis in glioblastoma. *Nat. Commun.* **14**, 4122 (2023).
22. J. M. Taube, A. Klein, J. R. Brahmer, H. Xu, X. Pan, J. H. Kim, L. Chen, D. M. Pardoll, S. L. Topalian, R. A. Anders, Association of PD-1, PD-1 ligands, and other features of the tumor immune microenvironment with response to anti-PD-1 therapy. *Clin. Cancer Res.* **20**, 5064–5074 (2014).
23. G. Mazzaachi, D. Madeddu, A. Falco, G. Bocchialini, M. Goldoni, F. Sogni, G. Armani, C. A. Lagrasta, B. Lorusso, C. Mangiaracina, R. Vilella, C. Frati, R. Alfieri, L. Ampolini, M. Veneziani, E. M. Silini, A. Ardizzoni, K. Urbanek, F. Aversa, F. Quaini, M. Tiseo, Low PD-1 expression in cytotoxic CD8⁺ tumor-infiltrating lymphocytes confers an immune-privileged tissue microenvironment in NSCLC with a prognostic and predictive value. *Clin. Cancer Res.* **24**, 407–419 (2018).
24. M. Shirasawa, T. Yoshida, Y. Shimoda, D. Takayanagi, K. Shiraishi, T. Kubo, S. Mitani, Y. Matsumoto, K. Masuda, Y. Shinno, Y. Okuma, Y. Goto, H. Horinouchi, H. Ichikawa, T. Kohno, N. Yamamoto, S. Matsumoto, K. Goto, S.-I. Watanabe, Y. Ohe, N. Motoi, Differential immune-related microenvironment determines programmed cell death protein-1/programmed death-ligand 1 blockade efficacy in patients with advanced NSCLC. *J. Thorac. Oncol.* **16**, 2078–2090 (2021).
25. J.-R. Lin, B. Izar, S. Wang, C. Yapp, S. Mei, P. M. Shah, S. Santagata, P. K. Sorger, Highly multiplexed immunofluorescence imaging of human tissues and tumors using t-CyCLF and conventional optical microscopes. *Elife* **7**, e31657 (2018).
26. S. Black, D. Phillips, J. W. Hickey, J. Kennedy-Darling, V. G. Venkataraman, N. Samusik, Y. Goltsve, C. M. Schürch, G. P. Nolan, CODEX multiplexed tissue imaging with DNA-conjugated antibodies. *Nat. Protoc.* **16**, 3802–3835 (2021).
27. S. He, R. Bhatt, C. Brown, E. A. Brown, D. L. Buhr, K. Chantranuvatana, P. Danaher, D. Dunaway, R. G. Garrison, G. Geiss, M. T. Gregory, M. L. Hoang, R. Khafizov, E. E. Killingsbeck, D. Kim, T. K. Kim, Y. Kim, A. Klock, M. Korukonda, A. Kutchma, Z. R. Lewis, Y. Liang, J. S. Nelson, G. T. Ong, E. P. Perillo, J. C. Phan, T. Phan-Everson, E. Piazza, T. Rane, Z. Reitz, M. Rhodes, A. Rosenblom, D. Ross, H. Sato, A. W. Wardhani, C. A. Williams-Wietzikoski, L. Wu, J. M. Beechem, High-plex imaging of RNA and proteins at subcellular resolution in fixed tissue by spatial molecular imaging. *Nat. Biotechnol.* **40**, 1794–1806 (2022).
28. M. H. Uddin, M. N. Al-Hallak, H. Y. Khan, A. Aboukameel, Y. Li, S. F. Bannoura, G. Dyson, S. Kim, Y. Mzzannar, I. Azar, T. Odisho, A. Mohamed, Y. Landesman, S. Kim, R. Beydoun, R. M. Mohammad, P. A. Philip, A. F. Shields, A. S. Azmi, Molecular analysis of XPO1 inhibitor and gemcitabine-nab-paclitaxel combination in KPC pancreatic cancer mouse model. *Clin. Transl. Med.* **13**, e1513 (2023).
29. K. S. S. Enfield, S. D. Martin, E. A. Marshall, S. H. Y. Kung, P. Gallagher, K. Milne, Z. Chen, B. H. Nelson, S. Lam, J. C. English, C. E. MacAulay, W. L. Lam, M. Guillaud, Hyperspectral cell sociology reveals spatial tumor-immune cell interactions associated with lung cancer recurrence. *J. Immunother. Cancer* **7**, 13 (2019).
30. M. Sorin, M. Rezanejad, E. Karimi, B. Fiset, L. Desharnais, L. J. M. Perus, S. Milette, M. W. Yu, S. M. Maritan, S. Doré, É. Pichette, W. Enlow, A. Gagné, Y. Wei, M. Orain, V. S. K. Manem, R. Rayes, P. M. Siegel, S. Camilleri-Broët, P. O. Fiset, P. Desmeules, J. D. Spicer, D. F. Quail, P. Joubert, L. A. Walsh, Single-cell spatial landscapes of the lung tumour immune microenvironment. *Nature* **614**, 548–554 (2023).
31. K. S. S. Enfield, E. Colliver, C. Lee, A. Magness, D. A. Moore, M. Sivakumar, K. Grigoriadis, O. Pich, T. Karasaki, P. S. Hobson, D. Levi, S. Veeriah, C. Puttick, E. L. Nye, M. Green, K. K. Dijkstra, M. Shimato, A. U. Akarca, T. Marafioti, R. Salgado, A. Hackshaw, TRACERx consortium, M. Jamal-Hanjani, F. van Maldegem, N. M. Granahan, B. Glass, H. Pulaski, E. Walk, J. L. Reading, S. A. Quezada, C. T. Hiley, J. Downward, E. Sahai, C. Swanton, M. Angelova, Spatial architecture of myeloid and T cells orchestrates immune evasion and clinical outcome in lung cancer. *Cancer Discov.* **14**, 1018–1047 (2024).
32. J. Monkman, A. Moradi, J. Yunis, G. Ivison, A. Mayer, R. Ladwa, K. O'Byrne, A. Kulasinghe, Spatial insights into immunotherapy response in non-small cell lung cancer (NSCLC) by multiplexed tissue imaging. *J. Transl. Med.* **22**, 239 (2024).
33. M. Sorin, E. Karimi, M. Rezanejad, M. W. Yu, L. Desharnais, S. A. C. McDowell, S. Doré, A. Arabzadeh, V. Breton, B. Fiset, Y. Wei, R. Rayes, M. Orain, F. Coulombe, V. S. K. Manem, A. Gagne, D. F. Quail, P. Joubert, L. A. Walsh, Single-cell spatial landscape of immunotherapy response reveals mechanisms of CXCL13 enhanced antitumor immunity. *J. Immunother. Cancer* **11**, e005545 (2023).
34. J. Chen, L. Larsson, A. Swarbrick, J. Lundeberg, Spatial landscapes of cancers: Insights and opportunities. *Nat. Rev. Clin. Oncol.* **21**, 660–674 (2024).
35. V. M. Ravi, P. Will, J. Kueckelhaus, N. Sun, K. Joseph, H. Salilé, L. Vollmer, U. Kuliesiute, J. von Ehr, J. K. Benotmane, N. Neidert, M. Follo, F. Scherer, J. M. Goeldner, S. P. Behringer, P. Franco, M. Khiat, J. Zhang, U. G. Hofmann, C. Fung, F. L. Ricklef, K. Lamsszu, M. Boerries, M. Ku, J. Beck, R. Sankowski, M. Schwabenland, M. Prinz, U. Schüller, S. Killmer, B. Bengsch, A. K. Walch, D. Delev, O. Schnell, D. H. Heiland, Spatially resolved multi-omics deciphers bidirectional tumor-host interdependence in glioblastoma. *Cancer Cell* **40**, 639–655.e13 (2022).
36. B. Weigelin, A. T. den Boer, E. Wagena, K. Broen, H. Dolstra, R. J. de Boer, C. G. Figgord, J. Textor, P. Friedl, Cytotoxic T cells are able to efficiently eliminate cancer cells by additive cytotoxicity. *Nat. Commun.* **12**, 5217 (2021).

37. A. Jevtic, J. Pantic, I. Jovanovic, M. Milovanovic, I. Stanojevic, D. Vojvodic, N. Arsenijevic, M. L. Lukic, G. D. Radosavljevic, Interleukin-33 pretreatment promotes metastatic growth of murine melanoma by reducing the cytotoxic capacity of CD8⁺ T cells and enhancing regulatory T cells. *Cancer Immunol. Immunother.* **69**, 1461–1475 (2020).
38. D. Zhang, H. Huang, X. Gao, G. Yu, X. Zhang, H. Jin, R. Xu, Z. Wang, G. Zhang, High expression of B7-H3 on monocyte/macrophages in tumor microenvironment promotes lung cancer progression by inhibiting apoptosis. *Transl. Oncol.* **41**, 101874 (2024).
39. J. Fang, Y. Lu, J. Zheng, X. Jiang, H. Shen, X. Shang, Y. Lu, P. Fu, Exploring the crosstalk between endothelial cells, immune cells, and immune checkpoints in the tumor microenvironment: New insights and therapeutic implications. *Cell Death Dis.* **14**, 586 (2023).
40. E. W. Roberts, M. L. Broz, M. Binnewies, M. B. Headley, A. E. Nelson, D. M. Wolf, T. Kaisho, D. Bogunovic, N. Bhardwaj, M. F. Krummel, Critical role for CD103⁺/CD141⁺ dendritic cells bearing CCR7 for tumor antigen trafficking and priming of T cell immunity in melanoma. *Cancer Cell* **30**, 324–336 (2016).
41. M. L. Broz, M. Binnewies, B. Boldajipour, A. E. Nelson, J. L. Pollack, D. J. Erle, A. Barczak, M. D. Rosenblum, A. Daud, D. L. Barber, S. Amigorena, L. J. Van't Veer, A. I. Sperling, D. M. Wolf, M. F. Krummel, Dissecting the tumor myeloid compartment reveals rare activating antigen-presenting cells critical for T cell immunity. *Cancer Cell* **26**, 638–652 (2014).
42. A. Hu, L. Sun, H. Lin, Y. Liao, H. Yang, Y. Mao, Harnessing innate immune pathways for therapeutic advancement in cancer. *Signal Transduct. Target. Ther.* **9**, 68 (2024).
43. L. Calderón, K. Schindler, S. G. Malin, A. Schebesta, Q. Sun, T. Schwickert, C. Alberti, M. Fischer, M. Jaritz, H. Tagoh, A. Ebert, M. Minnich, A. Liston, L. Cochella, M. Busslinger, Pax5 regulates B cell immunity by promoting PI3K signaling via PTEN down-regulation. *Sci. Immunol.* **6**, eabg5003 (2021).
44. J. P. Böttcher, C. Reis e Sousa, The role of type 1 conventional dendritic cells in cancer immunity. *Trends Cancer* **4**, 784–792 (2018).
45. J. P. Böttcher, E. Bonavita, P. Chakravarty, H. Blees, M. Cabeza-Cabrerozo, S. Sammicheli, N. C. Rogers, E. Sahai, S. Zelenay, C. Reis e Sousa, NK cells stimulate recruitment of cDC1 into the tumor microenvironment promoting cancer immune control. *Cell* **172**, 1022–1037.e14 (2018).
46. T. He, C. Tang, S. Xu, T. Moyana, J. Xiang, Interferon gamma stimulates cellular maturation of dendritic cell line DC2.4 leading to induction of efficient cytotoxic T cell responses and antitumor immunity. *Cell. Mol. Immunol.* **4**, 105–111 (2007).
47. K. C. Barry, J. Hsu, M. L. Broz, F. J. Cueto, M. Binnewies, A. J. Combes, A. E. Nelson, K. Loo, R. Kumar, M. D. Rosenblum, M. D. Alvarado, D. M. Wolf, D. Bogunovic, N. Bhardwaj, A. I. Daud, P. K. Ha, W. R. Ryan, J. L. Pollack, B. Samad, S. Asthana, V. Chan, M. F. Krummel, A natural killer-Dendritic cell axis defines checkpoint therapy-Responsive tumor microenvironments. *Nat. Med.* **24**, 1178–1191 (2018).
48. S. Graham, Q. D. Vu, S. E. A. Raza, A. Azam, Y. W. Tsang, J. T. Kwak, N. Rajpoot, Hover-Net: Simultaneous segmentation and classification of nuclei in multi-tissue histology images. *Med. Image Anal.* **58**, 101563 (2019).
49. S. Wang, R. Rong, D. M. Yang, J. Fujimoto, S. Yan, L. Cai, L. Yang, D. Luo, C. Behrens, E. R. Parra, B. Yao, L. Xu, T. Wang, X. Zhan, I. I. Wistuba, J. Minna, Y. Xie, G. Xiao, Computational Staining of pathology images to study the tumor microenvironment in lung cancer. *Cancer Res.* **80**, 2056–2066 (2020).
50. R. Rong, H. Sheng, K. W. Jin, F. Wu, D. Luo, Z. Wen, C. Tang, D. M. Yang, L. Jia, M. Amgad, L. A. D. Cooper, Y. Xie, X. Zhan, S. Wang, G. Xiao, A deep learning approach for Histology-based nucleus segmentation and tumor microenvironment characterization. *Mod. Pathol.* **36**, 100196 (2023).
51. R. Verma, N. Kumar, A. Patil, N. C. Kurian, S. Rane, S. Graham, Q. D. Vu, M. Zwager, S. E. A. Raza, N. Rajpoot, X. Wu, H. Chen, Y. Huang, L. Wang, H. Jung, G. T. Brown, Y. Liu, S. Liu, S. A. F. Jahromi, A. A. Khani, E. Montahaei, M. S. Baghshah, H. Behrooz, P. Semkin, A. Rassadin, P. Dutande, R. Lodaya, U. Baid, B. Baheti, S. Talbar, A. Mahbod, R. Ecker, I. Ellinger, Z. Luo, B. Dong, Z. Xu, Y. Yao, S. Lv, M. Feng, K. Xu, H. Zunair, A. B. Hamza, S. Smiley, T.-K. Yin, Q.-R. Fang, S. Srivastava, D. Mahapatra, L. Trnavska, H. Zhang, P. L. Narayanan, J. Law, Y. Yuan, A. Tejomay, A. Mitkari, D. Koka, V. Ramachandra, L. Kini, A. Sethi, MoNuSAC2020: A multi-organ nuclei segmentation and classification challenge. *IEEE Trans. Med. Imaging* **40**, 3413–3423 (2021).
52. J.-R. Lin, Y.-A. Chen, D. Campton, J. Cooper, S. Coy, C. Yapp, J. B. Tefft, E. McCarty, K. L. Ligon, S. J. Rodig, S. Reese, T. George, S. Santagata, P. K. Sorger, High-plex immunofluorescence imaging and traditional histology of the same tissue section for discovering image-based biomarkers. *Nat. Cancer* **4**, 1036–1052 (2023).
53. S. Zhao, D.-P. Chen, T. Fu, J.-C. Yang, D. Ma, X.-Z. Zhu, X.-X. Wang, Y.-P. Jiao, X. Jin, Y. Xiao, W.-X. Xiao, H.-Y. Zhang, H. Lv, A. Madabhushi, W.-T. Yang, Y.-Z. Jiang, J. Xu, Z.-M. Shao, Single-cell morphological and topological atlas reveals the ecosystem diversity of human breast cancer. *Nat. Commun.* **14**, 6796 (2023).
54. S. Hänselmann, R. Castelo, J. Guinney, GSVA: Gene set variation analysis for microarray and RNA-seq data. *BMC Bioinformatics* **14**, 7 (2013).
55. D. Planchard, S. Popat, K. Kerr, S. Novello, E. F. Smit, C. Fairve-Finn, T. S. Mok, M. Reck, P. E. Van Schil, M. D. Hellmann, S. Peters, Metastatic non-small cell lung cancer: ESMO clinical practice guidelines for diagnosis, treatment and follow-up. *Ann. Oncol.* **30**, 863–870 (2019).
56. E. R. Parra, J. Zhang, D. Y. Duose, E. Gonzalez-Kozlova, M. W. Redman, H. Chen, G. C. Manyam, G. Kumar, J. Zhang, X. Song, R. Lazcano, M. L. Marques-Piubelli, C. Laberiano-Fernandez, F. Rojas, B. Zhang, L. Taing, A. Jhaveri, J. Geisberg, J. Altreuter, F. Michor, J. Provencher, J. Yu, E. Cerami, R. Moravec, K. Kannan, R. Luthra, G. Alatrash, H.-H. Huang, H. Xie, M. Patel, K. Nie, J. Harris, K. Argueta, J. Lindsay, R. Biswas, S. Van Nostrand, S. Kim-Schulze, J. E. Gray, R. S. Herbst, I. I. Wistuba, S. Gettinger, K. Kelly, L. Bazhenova, S. Gnajtic, J. J. Lee, J. Zhang, C. Haymaker, Multi-omics analysis reveals immune features associated with immunotherapy benefit in patients with squamous cell lung cancer from Phase III Lung-MAP S14001 Trial. *Clin. Cancer Res.* **30**, 1655–1668 (2024).
57. S.-Y. Wu, S.-W. Zhang, D. Ma, Y. Xiao, Y. Liu, L. Chen, X.-Q. Song, X.-Y. Ma, Y. Xu, W.-J. Choi, X. Jin, Z.-M. Shao, Y.-Z. Jiang, CCL19⁺ dendritic cells potentiate clinical benefit of anti-PD-(L)1 immunotherapy in triple-negative breast cancer. *Med.* **4**, 373–393.e8 (2023).
58. M. Di Pilato, R. Kfuri-Rubens, J. N. Pruessmann, A. J. Ozga, M. Messenaker, B. L. Cadilha, R. Sivakumar, C. Cianciaruso, R. D. Warner, F. Marangoni, E. Carrizosa, S. Lesch, J. Billingsley, D. Perez-Ramos, F. Zavala, E. Rheinbay, A. D. Luster, M. Y. Gerner, S. Kobold, M. J. Pittet, T. R. Mempel, CXCR6 positions cytotoxic T cells to receive critical survival signals in the tumor microenvironment. *Cell* **184**, 4512–4530.e22 (2021).
59. J. Gamper, N. A. Koobbanani, K. Benes, S. Graham, M. Jahanifar, S. A. Khurram, A. Azam, K. Hewitt, N. Rajpoot, PanNuke Dataset Extension, Insights and Baselines. arXiv:2003.10778 [eess.IV] (2020).
60. G. Jaume, P. Doucet, A. H. Song, M. Y. Lu, C. Almagro-Pérez, S. J. Wagner, A. J. Vaidya, R. J. Chen, D. F. K. Williamson, A. Kim, F. Mahmood, HEST-1k: A Dataset for Spatial Transcriptomics and Histology Image Analysis. arXiv:2406.16192 [cs.CV] (2024).
61. E. Wu, M. Bieniosiek, Z. Wu, N. Thakkar, G. W. Charville, A. Makky, C. Schürch, J. R. Huyghe, U. Peters, C. I. Li, L. Li, H. Giba, V. Behera, A. Raman, A. E. Trevino, A. T. Mayer, J. Zou, ROSIE: AI generation of multiplex immunofluorescence staining from histopathology images. bioRxiv 2024.11.10.622859 [Preprint] (2024). https://doi.org/10.1101/2024.11.10.622859.
62. E. Wu, A. E. Trevino, Z. Wu, K. Swanson, H. J. Kim, H. B. D'Angio, R. Preska, A. E. Chiou, G. W. Charville, P. Dalerba, U. Duvvuri, A. D. Colevas, J. Levi, N. Bedi, S. Chang, J. Sunwoo, A. M. Egloff, R. Uppaluri, A. T. Mayer, J. Zou, 7-UP: Generating in silico CODEX from a small set of immunofluorescence markers. *PNAS Nexus* **2**, pgad171 (2023).
63. S. Andani, B. Chen, J. Ficek-Pascual, S. Heinke, R. Casanova, B. Hild, B. Sobottka, B. Bodenmüller, Tumor Profiler Consortium, V. H. Koelzer, G. Rätsch, HistoPlexer: Histopathology-based protein multiplex generation using deep learning. medRxiv 2024.01.26.24301803 [Preprint] (2024). https://doi.org/10.1101/2024.01.26.24301803.
64. J. Li, H. Liu, W. Liu, P. Zong, K. Huang, Z. Li, H. Li, T. Xiong, G. Tian, C. Li, J. Yang, Predicting gastric cancer tumor mutational burden from histopathological images using multimodal deep learning. *Brief. Funct. Genomics* **23**, 228–238 (2024).
65. J. N. Kather, A. T. Pearson, N. Halama, D. Jäger, J. Krause, S. H. Loosen, A. Marx, P. Boor, F. Tacke, U. P. Neumann, H. I. Grabsch, T. Yoshikawa, H. Brenner, J. Chang-Claude, M. Hoffmeister, C. Trautwein, T. Luedde, Deep learning can predict microsatellite instability directly from histology in gastrointestinal cancer. *Nat. Med.* **25**, 1054–1056 (2019).
66. S. J. Wagner, D. Reisenbüchler, N. P. West, J. M. Niehues, J. Zhu, S. Foersch, G. P. Veldhuizen, P. Quirke, H. I. Grabsch, P. A. van den Brandt, G. G. A. Hutchins, S. D. Richman, T. Yuan, R. Langer, J. C. A. Jenniskens, K. Offermans, W. Mueller, R. Gray, S. B. Gruber, J. K. Greenson, G. Renert, J. D. Bonner, D. Schmolze, J. Jonnagaddala, N. J. Hawkins, R. L. Ward, D. Morton, M. Seymour, L. Magill, M. Nowak, J. Hay, V. H. Koelzer, D. N. Church, TransSCOT consortium, C. Matek, C. Geppert, C. Peng, C. Zhi, X. Ouyang, J. A. James, M. B.oughrey, M. Salto-Tellez, H. Brenner, M. Hoffmeister, D. Truhn, J. A. Schnabel, M. Boxberg, T. Peng, J. N. Kather, Transformer-based biomarker prediction from colorectal cancer histology: A large-scale multicentric study. *Cancer Cell* **41**, 1650–1661.e4 (2023).
67. G. Shamai, A. Livne, A. Polónia, E. Sabo, A. Cretu, G. Bar-Sela, R. Kimmel, Deep learning-based image analysis predicts PD-L1 status from H&E-stained histopathology images in breast cancer. *Nat. Commun.* **13**, 6753 (2022).
68. J. Hu, C. Cui, W. Yang, L. Huang, R. Yu, S. Liu, Y. Kong, Using deep learning to predict anti-PD-1 response in melanoma and lung cancer patients from histopathology images. *Transl. Oncol.* **14**, 100921 (2021).
69. K. Saednia, A. Lagree, M. A. Alera, L. Fleshner, A. Shiner, E. Law, B. Law, D. W. Dodington, F.-I. Lu, W. T. Tran, A. Sadeghi-Naini, Quantitative digital histopathology and machine learning to predict pathological complete response to chemotherapy in breast cancer patients using pre-treatment tumor biopsies. *Sci. Rep.* **12**, 9690 (2022).
70. S. Steyaert, Y. L. Qiu, Y. Zheng, P. Mukherjee, H. Vogel, O. Gevaert, Multimodal deep learning to predict prognosis in adult and pediatric brain tumors. *Commun. Med. (Lond)* **3**, 44 (2023).
71. L. H. Schwartz, S. Litière, E. de Vries, R. Ford, S. Gwyther, S. Mandrekar, L. Shankar, J. Bogaerts, A. Chen, J. Dancey, W. Hayes, F. S. Hodis, O. S. Hoekstra, E. P. Huang, N. Lin, Y. Liu, P. Therasse, J. D. Wolchok, L. Seymour, RECIST 1.1-Update and clarification: From the RECIST committee. *Eur. J. Cancer* **62**, 132–137 (2016).
72. M. Weigert, U. Schmidt, R. Haase, K. Sugawara, G. Myers, in 2020 IEEE Winter Conference on Applications of Computer Vision (WACV) (IEEE, 2020).

73. Cancer Genome Atlas Research Network, Comprehensive molecular profiling of lung adenocarcinoma. *Nature* **511**, 543–550 (2014).
74. Cancer Genome Atlas Research Network, Comprehensive genomic characterization of squamous cell lung cancers. *Nature* **489**, 519–525 (2012).
75. M. Pizurica, Y. Zheng, F. Carrillo-Perez, H. Noor, W. Yao, C. Wohlfart, A. Vladimirova, K. Marchal, O. Gevaert, Digital profiling of gene expression from histology images with linearized attention. *Nat. Commun.* **15**, 9886 (2024).
76. R. Patro, G. Duggal, M. I. Love, R. A. Irizarry, C. Kingsford, Salmon provides fast and bias-aware quantification of transcript expression. *Nat. Methods* **14**, 417–419 (2017).
77. A. M. Newman, C. B. Steen, C. L. Liu, A. J. Gentles, A. A. Chaudhuri, F. Scherer, M. S. Khodadoust, M. S. Esfahani, B. A. Luca, D. Steiner, M. Diehn, A. A. Alizadeh, Determining cell type abundance and expression from bulk tissues with digital cytometry. *Nat. Biotechnol.* **37**, 773–782 (2019).
78. M. I. Love, W. Huber, S. Anders, Moderated estimation of fold change and dispersion for RNA-seq data with DESeq2. *Genome Biol.* **15**, 550 (2014).
79. Z. Fang, X. Liu, G. Peltz, GSEApY: A comprehensive package for performing gene set enrichment analysis in Python. *Bioinformatics* **39**, btac757 (2023).

Acknowledgments: Figure 5 was created using BioRender.com. **Funding:** We are grateful for the support from Owkin Inc. for this project. Research reported here was further supported by the National Cancer Institute (NCI) under the awards R01 CA260271 (O.G.). The content is solely

the responsibility of the authors and does not necessarily represent the official views of the National Institutes of Health. **Author contributions:** Conceptualization: Y.Z. and O.G. Methodology: Y.Z. and O.G. Investigation: Y.Z., C.S., M.O., B.E.H., and O.G. Visualization: Y.Z. Supervision: O.G. Writing—original draft: Y.Z. Writing—review and editing: Y.Z., C.S., M.O., B.E.H., and O.G. **Competing interests:** A provisional patent application (no. 63/564,920), titled “AI-Driven Prediction of Therapeutic Response in Non-Small-Cell Lung Cancer from Histology Images,” was filed with the US Patent and Trademark Office on 13 March 2024 (inventors: Y.Z. and O.G.). All other authors declare that they have no competing interests. **Data and materials availability:** All data needed to evaluate the conclusions in the paper are present in the paper and/or the Supplementary Materials. mIF imaging data, deidentified clinical information, and nucleus segmentation and cell-type classification results from whole-slide H&E-stained histology images are available on Dryad with doi: 10.5061/dryad.b8gtht7p4. Single-sample gene set enrichment scores from RNA-seq data are available on Dryad with doi: 10.5061/dryad.b8gtht7p4. The model weights for NucSegAI are publicly available in the Hugging Face repository (<https://huggingface.co/OGevaertLab/NucSegAI>). The code used for analysis is available on Zenodo (doi: 10.5061/dryad.b8gtht7p4) and GitHub (<https://github.com/gevaertlab/sc-lung>).

Submitted 30 October 2024

Accepted 22 April 2025

Published 23 May 2025

10.1126/sciadv.adu2151